Annu. Rev. Phys. Chem. 2006. 57:555–92
doi: 10.1146/annurev.physchem.57.032905.104601

FEMTOSECOND TIME-RESOLVED PHOTOELECTRON IMAGING

Toshinori Suzuki
Chemical Dynamics Laboratory, RIKEN (Institute of Physical and Chemical Research), Wako 351-0198, Japan; email: toshisuzuki@riken.jp

Key Words ultrafast spectroscopy, wave-packet dynamics, photoionization-differential cross sections, photoelectron-angular distribution

■ **Abstract** Femtosecond time-resolved photoelectron imaging (TRPEI) is a variant of time-resolved photoelectron spectroscopy used in the study of gas-phase photoinduced dynamics. A new observable, time-dependent photoionization-differential cross section provides useful information on wave-packet motions, electronic dephasing, and photoionization dynamics. This review describes fundamental issues and the most recent works involving TRPEI.

INTRODUCTION AND OVERVIEW

The fine details of bimolecular chemical–reaction dynamics have been experimentally studied using the crossed-molecular beam method (1, 2). This sophisticated method measures the (state-resolved) differential cross sections (DCSs), i.e., the scattering and quantum-state distributions of reaction products (3–5), for well-defined initial states of reagents at controlled collision energies. The DCS and excitation function (the collision energy dependence of the reaction) are valuable in elucidating a reaction mechanism (6, 7), especially when compared with accurate theoretical predictions (8–10). On the other hand, the crossed-molecular beam method observes asymptotic states of products, not the dynamics at short interparticle distances, as in the case of elementary particle physics. The quest for direct experimental observation of electron and nuclear motions in reaction is a driving factor behind the development of ultrafast-laser spectroscopy (11).

According to the Born-Oppenheimer approximation, which is widely applicable to various molecular problems, chemical reactions are driven primarily by electrons. Real-time observation of a nonstationary electronic state or electron orbitals in chemical transformation is essential for elucidation of the reaction mechanism. From this viewpoint, femtosecond time-resolved photoelectron spectroscopy (TRPES), which probes electronic states with femtosecond time resolution, is extremely useful. Furthermore, ionization can occur from any electronic state and in any nuclear geometry, provided the ionization wavelength is sufficiently short.

Therefore, TRPES serves as a versatile means to probe dynamics along the entire reaction pathway.

Photoionization is inherently an electron-scattering process, in which the most detailed observable is the photoionization DCS. Conventional photoelectron spectroscopy has employed photoelectron-angular distribution (PAD) to investigate the ionization continuum, including such features as the autoionization resonance (12), shape resonance (13), and Cooper minimum (14, 15). However, TRPES did not fully exploit time-dependent PAD as an observable until recently. In 1999, two research groups presented femtosecond time-resolved photoelectron imaging (TRPEI) to visualize time-dependent photoionization DCS (16–20). Since then TRPEI has been applied to various molecular systems including large molecular aggregates (21, 22).

The characteristics of TRPEI—or more generally TRPES—may be understood in comparison with other means of probing electronic states or electron orbitals. The X-ray free-electron lasers that are planed or under construction in several countries (23) will enable ultrafast X-ray diffraction (and scattering) with femtosecond time resolution (24, 25). Because X-ray diffraction depends on the total electron-density distribution in a molecule, it is utilized for the direct determination of nuclear positions. Ultrafast X-ray diffraction is expected to significantly impact studies of complex systems including biological molecules (26), and its development is anticipated to progress considerably over the next 5 years. For an analogous approach of ultrafast-electron diffraction, see the review by Zewail in this volume (26a). On the other hand, chemical dynamics often require information on a specific electron orbital that plays a key role in the reaction. The (e, 2e) momentum spectroscopy (27, 28) can observe distribution functions of various electron orbitals in the momentum space, even in the frame of a molecule in its most advanced form (29). However, its signal level is extremely low and an ultrafast pump-probe experiment has not been realized with (e, 2e). Itatani et al. (30) have presented a novel approach to realize tomographic imaging of a molecular orbital using high harmonic generation in an intense laser field (31–33). This method utilizes recollision of an electron that is tunnel-ionized from a molecule and accelerated in a laser field to facilitate the 1D Fourier transform of the function $\vec{r}\psi_{HOMO}(\vec{r})$ (HOMO is the highest occupied molecular orbital), from which $\psi_{HOMO}(\vec{r})$ can be reconstructed. The applicability of this method to chemical dynamics is to be studied further. An important consideration in the ultrafast pump-probe experiment is whether the probing step selectively monitors the photoexcited molecules. This is important from a practical viewpoint because a pump pulse does not typically excite all the molecules in the target volume; in fact, most of the molecules remain unexcited. If the probing step is nonselective, the observed signal will be overwhelmed by the unexcited ground-state molecules. Although the signal of interest can be extracted by taking the difference between the data obtained with and without the pump pulses, this procedure is not always accurate. TRPES of neutral molecules with visible and UV probe light selectively observes an ensemble of molecules excited by the pump pulses, thus making this approach sensitive and straightforward.

This review focuses on TRPEI, the time-dependent PAD, and related subjects with examples from works in the last few years. The reader is referred to other excellent articles from the *Annual Review of Physical Chemistry* (34–38) and elsewhere (39–43) for a general historical background on TRPES and the literature up until 2003.

PHOTOELECTRON IMAGING

In this section, I provide only a brief explanation of photoelectron imaging (PEI) because the technical details of TRPEI are beyond the scope of this review. PEI involves the 2D multiplex detection of the velocity vectors of electrons. Although multiplex detection takes place in many other experiments in various disciplines, PEI has essentially been derived from cold target–recoil ion-momentum spectroscopy in atomic physics (44, 45) and 2D photofragment ion–imaging in physical chemistry (46, 47). The ion-imaging apparatus reported by Chandler & Houston (46) is largely the same as the Wiley-McLaren time-of-flight mass spectrometer (48), except that an electron multiplier at the end of the flight tube is replaced with a 2D position-sensitive detector. Helm, Jung, and their coworkers (49–51) performed PEI with nanosecond lasers in the mid-1990s. The acceleration electrodes modified by Eppink & Parker (52) provided an immersion lens for 2D space focusing of charged-particle trajectories; the arrival positions of particles depend only on their velocity and not the initial position (the velocity map imaging). Further modification of the electrodes by Wrede et al. (53) minimized chromatic and spherical aberrations in charged-particle trajectories, thus improving the imaging resolution. Magnification and contraction of electron images is possible by either changing the time-of-flight or by bending the electron trajectories with an electrostatic lens placed in the middle of the flight tube (54–56): Garcia et al. (56) observed electrons having kinetic energies of up to 14 eV with an energy resolution of 6%. Weber et al. (57) combined a retarding electric field with a solenoidal-magnetic guiding field to achieve resolution of <1eV at 300 eV.

A camera-based system and a delay line detector (58) are commonly employed as 2D position-sensitive detectors in PEI. Both comprise a microchannel plate as the front surface, and each photoelectron that impinges upon the detector induces the secondary electron amplification in a 5–12-μm microchannel. The amplified electron pulses are emitted from the back of the microchannel plate. However, the method of obtaining 2D positions of amplified electron pulses differs between the two systems. In the camera-based system, electron pulses are accelerated toward a phosphor screen at kinetic energies up to 2–4 keV. Light spots on the screen are observed by a charge-coupled device or a complementary metal-oxide semiconductor camera. The latter can capture images at a high-frame rate comparable with the repetition rate of amplified femtosecond laser systems. The delay line detector places finely spaced wires (delay lines) on the back of the microchannel plate and measures the transmission times of the electric pulses through these lines. The

2D positions are then calculated using these measurements. The delay line detector registers both the arrival position and the arrival time; however, it can handle only up to 4 to 5 electrons in a response time of approximately 10 ns. In contrast, there is virtually no limit to the number of electrons that the camera-based system can detect simultaneously; however, the camera-based system cannot record the arrival times of electrons. This system is mainly used in photoionization experiments with lasers where many electrons are created. Another advantage of the camera-based system is the realization of high-fidelity measurements, as described below. Moreover, imaging resolution is improved to subpixel resolution (59) by real-time image processing (centroiding of each light spot) of each frame (59–61). A drawback of camera-based TRPEI is that a cylindrical symmetry of the 3D distribution is required to reconstruct a single image, which restricts the pump and probe laser polarization to be parallel to each other. The reconstruction is usually performed by an inverse Abel transform, although basis-set expansion methods are more robust to numerical noises in image data (62, 63). A monograph describes useful tutorials (47), and some more recent approaches can be found in the literature (63–65).

ROTATIONAL WAVE-PACKET AND PHOTOELECTRON-ANGULAR ANISOTROPY

Various dynamics in the neutral state affect PAD. For instance, when the system undergoes a nonadiabatic transition, ionization transition–dipole moments to the continuum wave functions vary with the wave-packet motion, creating a time-dependent PAD (66, 67). However, nonadiabatic transitions in isolated molecules and clusters are generally associated with a change in the vibrational wave function, which can be observed in the time-dependent photoelectron kinetic energy distribution (PKED). Although TRPEI offers the most efficient measurement of a time-dependent PKED via the ultimate collection efficiency (100%) of photoelectrons, PKED is measurable with conventional TRPES. Therefore, to illustrate the unique features of TRPEI, we concentrate on a time-dependent PAD and the directional properties of a molecule in this section.

A molecular orbital is inherently anisotropic, and ejection of an electron from the molecular orbital creates a complex molecular-frame photoelectron-angular distribution (MF-PAD). However, the laboratory-frame photoelectron-angular distribution (LF-PAD) is averaged over the molecular-axis distribution at the instant of ionization; thus the LF-PAD is generally less structured than the MF-PAD. Assuming that molecules are in the $J = 0$ state, this ensemble has no specific direction of the molecular axes in space, and it appears to be an isotropic target for ionization light. Such an isotropic ensemble provides only a weakly polarized LF-PAD from which hardly any detailed information on the molecular frame (MF) can be obtained.

In TRPEI, one-photon electronic transition in the pump step coherently excites the $P(\Delta J = -1)$, $Q(0)$, and $R(+1)$ branch lines. This creates a nonstationary superposition of the molecular rotational eigenstates or a rotational wave packet (68, 69). The wave packet provides a time-dependent molecular-axis distribution that revives at characteristic time intervals determined by rotational constants. The time-dependent molecular-axis distribution is generally expressed in terms of spherical harmonics (and the multipole moments):

$$P(t, \theta'_z, \phi'_z) = \sum_{KQ} A_{KQ}(t) Y_{KQ}(\theta'_z, \phi'_z), \qquad 1.$$

where θ'_z and ϕ'_z are the polar and azimuthal angles of the molecular axis, respectively, measured in the laboratory frame (LF). The odd K terms discriminate the molecular axes in the upward and downward directions and are referred to as the orientation terms, whereas the even K terms are referred to as the alignment terms. The orientation is not created by linearly polarized light. In one-photon photoexcitation of randomly oriented molecules by linearly polarized light, the highest rank K is 2, and the terms with $Q \neq 0$ vanish as a result of a cylindrical symmetry around the polarization of light:

$$P(t, \theta'_z, \phi'_z) = A_{00}(t) Y_{00}(\theta'_z, \phi'_z) + A_{20}(t) Y_{20}(\theta'_z, \phi'_z). \qquad 2.$$

The highest rank (K) in the equation is $K_{max} = 2n$ in the n-photon absorption process.

PAD is the flux distribution of the outgoing electrons as a function of their angle from the symmetry axis (the polarization direction of linearly polarized light or the propagation direction of circularly polarized light). In one-photon ionization of a randomly oriented ensemble of molecules with linearly polarized light, the LF-PAD is expressed by the following equation:

$$\frac{d\sigma}{d\Omega'_k} = \frac{\sigma}{4\pi}[1 + \beta P_2(\cos\theta'_k)], \qquad 3.$$

where θ'_k is the polar angle of the photoelectron $\boldsymbol{k}$-vector with respect to the ionization laser polarization, and $P_n(x)$ is a Legendre polynomial. When the ensemble of molecules is polarized as expressed by Equation 2, one-photon ionization of this ensemble with the probe-laser polarization parallel to that of the pump laser provides the following LF-PAD:

$$\frac{d\sigma(t)}{d\Omega'_k} = \frac{\sigma(t)}{4\pi}[1 + \beta_2(t) P_2(\cos\theta'_k) + \beta_4(t) P_4(\cos\theta'_k)]. \qquad 4.$$

Comparing Equations 3 and 4, the P_4 term in the $(1 + 1')$ resonance-enhanced multiphoton ionization (REMPI) appears only when the ionized target is anisotropic. In fact, $\sigma(t) \cdot \beta_4(t)$ is proportional to $A_{20}(t)$ in the $(1 + 1')$ REMPI. In general cases, including the pump and the probe laser not polarized in parallel, the PAD is expressed by (70)

$$\frac{d\sigma(t)}{d\Omega'_k} = \sum_{LQ} \beta_{LQ}(t) Y_{LQ}(\theta'_k, \phi'_k), \qquad 5.$$

where the maximum value of L is $2(m + n)$ in $(m + n)$ REMPI.

The photoelectron-anisotropy parameters can be expanded by the axis-alignment parameters as follows (71):

$$\beta_{LQ}(t) = \sum_{K} A_{K-Q}(t)\, a_{KLQ}, \qquad 6.$$

where the expansion coefficients a_{KLQ} carry all the information of photoionization dynamics. The detailed form of a_{KLQ} has been obtained by Underwood & Reid (71). In 2005, Suzuki & Seideman (57) presented a general quantum-mechanical expression for TRPEI, in which they show the relation between the time-dependent alignment moments and the rotational wave-packet revivals for various pump intensities. Under certain (realistic) conditions, the general expression (72) can be reduced to Equation 6. Several important points are noted for Equation 6. First, following $A_{KQ}(t)$, $\beta_{LQ}(t)$ also exhibits rotational wave-packet revival structures, provided a_{KLQ} are not too small. Second, if β_{LQ} are measured for known A_{KQ}, a_{KLQ} (or the ionization-dynamical parameters) can be determined. Finally, if a_{KLQ} are known and β_{LQ} are measured, A_{KQ} or the axis distribution can be determined.

Because photoelectron-scattering wave functions in the ionization continuum are degenerate, ionization is induced via various transition-dipole moments in MF: For instance, ionization can occur with comparable efficiencies via parallel and perpendicular transitions in linear molecules. Consequently, the ionization intensity (an integral cross section) in the $(1 + 1')$ scheme is rather insensitive to the rotational wave-packet motion, except that ionization is mediated by the autoionization resonance or shape resonance.

Rotational coherence spectroscopy monitors the periodic motion of a rotational wave packet through polarized fluorescence or transient absorption to higher electronic states: Other variants of rotational coherence spectroscopy, although not including TRPEI, have been considered by Felker & Zewail (73). An advantage of TRPEI in detecting rotational wave-packet dynamics is that photoionization is more sensitive than fluorescence. Bragg et al. (74) demonstrated the $(1 + 1')$ TRPEI detection of a rotational wave packet of C_2^- whose density in the ion beam is small. TRPEI can also observe wave packets in the triplet state, as described in the section below.

ROTATIONAL DYNAMICS IN ELECTRONIC DEPHASING

Polyatomic molecules hardly exhibit the unit fluorescence quantum yield because radiationless transitions (75) such as spin-allowed internal conversion and spin-forbidden intersystem crossing (ISC) are ubiquitous. The S_1−T_1 ISC in pyrazine is the best-known example for the intermediate coupling case in molecular radiationless transition (76–83). Strong spin-orbit coupling of the S_1 $B_{3u}(n\pi^*)$ vibronic state with moderately dense triplet vibronic states results in a complex energy structure of molecular eigenstates. Coherent excitation of these eigenstates creates a nonstationary state that rapidly evolves with time. The evolution has previously been monitored by fluorescence from the S_1 state, which exhibited a biexponential decay; the fast component is a result of pure dephasing between the component eigenstates, whereas the slow component is a result of depopulation of these eigenstates through deactivation down to S_0. On the other hand, there has been no direct detection of the dark manifold with ultrafast lasers.

The real-time observation of the S_1 decay and the T_1 formation was performed by TRPEI as shown in Figure 1. These images are doubly differential ionization cross section at specified pump-probe time delays. Because ionization occurs from the S_1 zero vibrational level to the low vibrational states of the cation due to the Franck-Condon overlap, the singlet component of the nonstationary state creates well-resolved concentric rings in the outer part of the photoelectron images (Figure 1*b*). On the other hand, as the origin of T_1 is located 0.5 eV (4055 cm^{-1}) lower than S_1, T_1 vibronic levels isoenergetic to the S_1 zero level are highly vibrationally excited. Consequently, ionization occurs from the T_1 vibronic levels to highly vibrationally excited levels of the cation at longer time delays, creating slow electrons that appear at the center of the images. The S_1 decay and the T_1 formation were found to occur with the identical time constant of 110 ps. Integration of the images for the angular part provides the time-dependent PKEDs displayed in Figure 1*c*. An isosbestic point was identified in the PKEDs at approximately 200 meV, illustrating that ISC is an exclusive decay process from S_1 in this time range. Vibrational structures in the PKED are attributed to progressions of totally symmetric vibrational modes. The PAD at individual photoelectron kinetic energies (PKEs) can be extracted from the images; for instance, the PADs associated with ionization from the S_1 zero level to the $6a^1$ level of the cation (the second outermost ring in Figure 1*b*) are presented as a function of the pump-probe time delay in Figure 1*a*. The PAD exhibits time dependence—it is slightly enhanced at $\theta_k' = 90^\circ$ only when $t = 0$ and at 82 ps (the first full revival time of the rotational wave packet). Correspondingly, the β_4 coefficients extracted from a series of the photoelectron images clearly exhibited the wave-packet revivals (42).

Although $(1 + 1')$ TRPEI is useful for probing rovibronic dynamics, a low-energy tail of the PKED from S_1 overlaps the PKED from T_1 in the $(1 + 1')$ REMPI (Figure 1*c*). An alternative way to selectively observe ionization from different electronic states is $(1 + 2')$ REMPI, where ionization occurs using Rydberg states as stepping stones (20, 84). As a result of the $\Delta v = 0$ propensity rule in ionization from the Rydberg states to the cation, this ionization scheme creates well-separated PKEDs for ionization from S_1 and T_1. Ionization from S_1 was observed through the singlet $3p_z(n^{-1})$ ($T_R = 55\,000\ \mathrm{cm}^{-1}$) and $3s(n^{-1})$ ($T_R = 50\,700\ \mathrm{cm}^{-1}$) Rydberg states, and ionization from T_1 occurred via the triplet $3s(n^{-1})$ ($T_R = 50\,200\ \mathrm{cm}^{-1}$) (Figure 2) (85). The *z*-axis of pyrazine in D_{2h} point group is along the *N*-*N* axis. The ionization intensities from the singlet state diminish with $\tau = 110 \pm 5$ ps, whereas that from the triplet grows accordingly. The rotational revival features in the singlet and triplet manifold are seen as rapid modulations in the intensities and anisotropy parameters. As the S_1 ($^1B_{3u}$) $\leftarrow$ S_0 (^1A_g) transition-dipole moment is parallel to the top axis of this near oblate-top molecule, the axis distributes as $\cos^2\theta_z'$

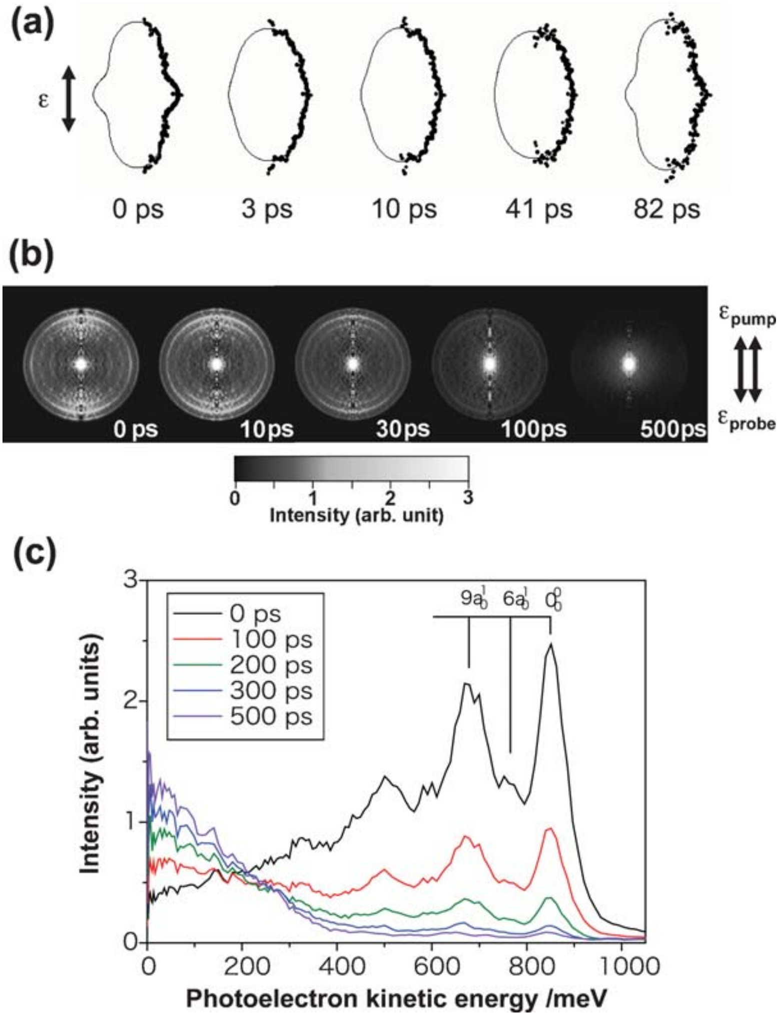

Figure 1 Time-resolved photoelectron images, photoelectron-angular distributions, and photoelectron kinetic energy distributions in $(1 + 1')$ resonance-enhanced multiphoton ionization via the S_1 zero vibrational level. The pump-laser wavelength was fixed to the (0, 0) band of the S_1 $(^1B_{3u}) \leftarrow S_0$ (^1A_g) transition (324 nm), and the probe-laser wavelength was 197 nm. (*a*) Polar plots of the photoelectron-angular distributions associated with ionization from the S_1 zero vibrational level to the cation $6a^1$ vibrational level at specified time delays. (*b*) Inverse Abel transforms of the time-resolved photoelectron images corresponding to the slices through the 3D photoelectron velocity distributions at specified time delays. (*c*) Photoelectron kinetic energy distributions obtained by angular integration of the inverse Abel transforms of the time-resolved photoelectron images. Structured distribution in the high energy side is a result of ionization from the S_1 state, whereas a low energy distribution appearing at long pump-probe time delays is ionization from T_1.

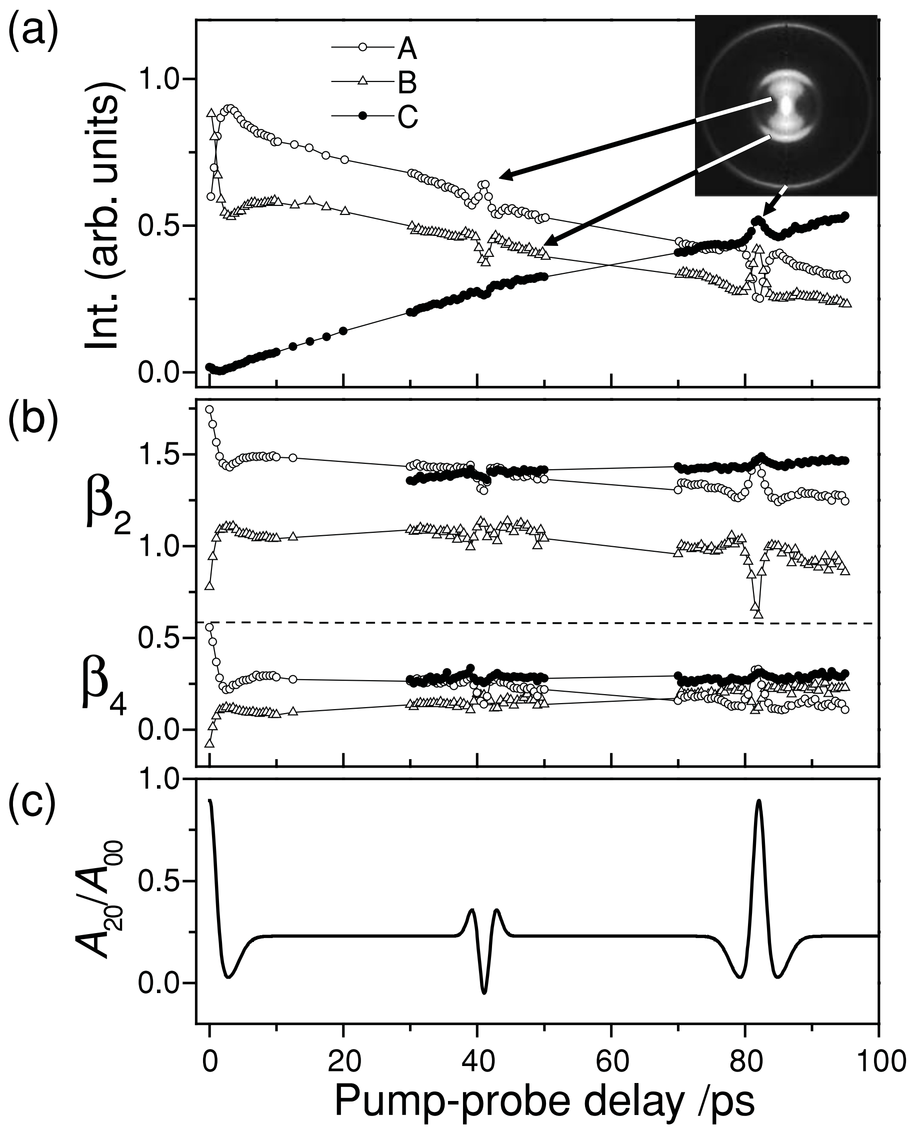

Figure 2 (*a*) Temporal profiles of the energy-selected photoelectron intensities in the (1 + 2′) resonance-enhanced multiphoton ionization of pyrazine via the S_1 zero vibrational level with the pump (324 nm) and probe (401 nm) lasers. A and B indicate S_1 detected via the $3p_z$ Rydberg state and S_1 via the 3s Rydberg state, respectively. C indicates T_1 detected via the 3s Rydberg state. (*b*) Time evolution of the anisotropy parameters, β_2 and β_4, of the photoelectron-angular distributions: $\beta_L = \sqrt{2L+1}\beta_{L0}$. (*c*) The alignment parameter, A_{20}/A_{00}, in the S_1 state calculated for the rotational temperature of 20 K.

with respect to the laser polarization at $t = 0$ and the full revival times. The revival features in the ionization intensities via $3s(n^{-1})$ and $3p_z(n^{-1})$ are out of phase, in which the former takes the maximum at $t = 0$. This unambiguously indicates that the transition-dipole moments for $3s \leftarrow S_1$ and $3p_z \leftarrow S_1$ are parallel and perpendicular to the top axis, respectively. The $3p_z \leftarrow S_1$ transition is vibronically induced, as it is an *ungerade-ungerade* electronic transition. The revival features in anisotropy parameters are also out of phase in ionization via $3s(n^{-1})$ and $3p_z(n^{-1})$; however this is for a different reason. The time-dependent anisotropy parameters indicate that the MF-PAD has a sharper peak in the parallel than in the perpendicular ionization transition from 3s, whereas this relation is reversed in ionization from $3p_z$. The analysis of the time dependencies of anisotropy parameters provided the LF-PADs expected for the axis alignment of $\cos^4\theta_z'$ and $\sin^4\theta_z'$, which exhibited dramatic differences from each other (86).

The revival feature appears quite strongly in the singlet signal, both in the intensities and the photoelectron-angular anisotropies, whereas the revival feature is considerably smaller for the triplet. In 2004 Tsubouchi et al. (86) theoretically examined the rotational revival feature in ionization from the T_1 state. In the analysis, pyrazine was approximated as an oblate symmetric top because the asymmetry parameter is 0.985 in the 0^0 level in S_1 (87). The triplet state—with a small spin splitting—was described by Hund's coupling case b, whereas the singlet state was described by case a. The basis sets for these two cases are denoted as $|NJKSM\rangle$ and $|JPM\rangle|S\Sigma\rangle$, respectively (88). The quantum numbers are as follows: N denotes the rotational angular momentum, J the total angular momentum, K the projection of N on the top axis, S the spin-angular momentum, M the projection of J on the space-fixed axis, P the projection of J on the top axis, and Σ the projection of S on the top axis. The analogy with the diatomic case is such that J, N, K, and P correspond to J, N, Λ, and Ω, where Λ and Ω are the projection quantum numbers of the electronic orbital and the total angular momenta onto the internuclear axis, respectively. The molecular eigenstates of the effective Hamiltonian, including the spin-orbit coupling, are expressed by a linear combination of the zero-order S_1 and T_1 states:

$$|n\rangle_{J_S P_S M_S} = a_n^{J_S P_S M_S}|\Gamma_S, 0\rangle|J_S P_S M_S\rangle|0, 0\rangle + \sum_{iN_T K_T} b_n^{iN_T K_T M_S}\left|\Gamma_T, v_T^i\right\rangle|N_T J_S K_T 1 M_S\rangle, \qquad 7.$$

where v^i represents the vibrational quantum number of the i-th mode, and Γ_i includes all other quantum numbers. The zero-order eigenenergies of the S_1 states were constructed from the spectroscopic constants in the literature (87), whereas those of the T_1 states remained unknown. Accordingly, the T_1 vibronic levels were randomly distributed around the S_1 0^0 level with a state density of ρ that reproduces the observed dephasing time. The weighting factors, $a_n^{J_S P_S M_S}$ and $b_n^{iN_T K_T M_S}$, and the eigenenergies, $E_n^{J_S P_S M_S}$, were obtained by diagonalizing the Hamiltonian matrix.

The time-dependent wave function of the nonstationary state is expressed by

$$\Psi(\Omega'; t; J_0 P_0 M_0) \propto \sum_{J_\mathrm{S} P_\mathrm{S} M_\mathrm{S}} I(J_\mathrm{S} P_\mathrm{S} M_\mathrm{S}; J_0 P_0 M_0) \times \sum_n a_n^{J_\mathrm{S} P_\mathrm{S} M_\mathrm{S}} |n\rangle_{J_\mathrm{S} P_\mathrm{S} M_\mathrm{S}} \exp\left(-i E_n^{J_\mathrm{S} P_\mathrm{S} M_\mathrm{S}} t \big/ \hbar\right), \qquad 8.$$

where $I(J_\mathrm{S} P_\mathrm{S} M_\mathrm{S}; J_0 P_0 M_0)$ denotes the excitation strength from a rotational state $|J_0 P_0 M_0\rangle$ in the S_0 zero vibrational level to each $|J_\mathrm{S} P_\mathrm{S} M_\mathrm{S}\rangle$. The singlet and triplet components of the nonstationary state are

$$\Psi_\mathrm{S}(\Omega'; t; J_0 P_0 M_0) = \sum_{J_\mathrm{S}} |\Gamma_\mathrm{S}, 0\rangle\, |J_\mathrm{S} P_0 M_0\rangle\, |0, 0\rangle \times \langle \Gamma_\mathrm{S}, 0 | \langle J_\mathrm{S} P_0 M_0 | \langle 0, 0 | \Psi(\Omega'; t; J_0 P_0 M_0)\rangle\rangle \qquad 9.$$

and

$$\Psi_\mathrm{T}(\Omega'; t; J_0 P_0 M_0) = \sum_{i\, J_\mathrm{S} N_\mathrm{T} K_\mathrm{T}} |N_\mathrm{T} J_\mathrm{S} K_\mathrm{T} 1 M_0\rangle \left|\Gamma_\mathrm{T}, v_\mathrm{T}^\mathrm{i}\right\rangle \times \langle N_\mathrm{T} J_\mathrm{S} K_\mathrm{T} 1 M_0 | \left\langle \Gamma_\mathrm{T}, v_\mathrm{T}^\mathrm{i} \right| \Psi(\Omega'; t; J_0 P_0 M_0)\rangle\rangle, \qquad 10.$$

respectively. The distribution function of the top axes in the S_1 and T_1 states are

$$P^\mathrm{S}(\theta_z'; t; T_{rot}) = \sum_{J_0 K_0 M_0} \exp\left(-E^{rot}_{J_0 K_0 M_0} \big/ k_B T_{rot}\right) \times \iint d\phi\, d\chi\, \Psi_S^*(\Omega'; t; J_0 P_0 M_0) \Psi_\mathrm{S}(\Omega'; t; J_0 P_0 M_0) \qquad 11.$$

and

$$P^\mathrm{T}(\theta_z'; t; T_{rot}) = \sum_{J_0 K_0 M_0} \exp\left(-E^{rot}_{J_0 K_0 M_0} \big/ k_B T_{rot}\right) \times \iint d\phi\, d\chi\, \Psi_T^*(\Omega'; t; J_0 P_0 M_0) \Psi_\mathrm{T}(\Omega'; t; J_0 P_0 M_0), \qquad 12.$$

respectively, where k_B is the Boltzmann constant, T_{rot} is the rotational temperature in the molecular beam, and $E^{rot}_{J_0 K_0 M_0}$ is the rotational energy of the $|J_0 P_0 M_0\rangle$ state. The experimental result was well reproduced by the calculations (Figure 3).

The mechanism that reduces the revival signal in the dark state was explained as follows (Figure 4). For simplicity, we first discuss the case of intramolecular vibrational redistribution via anharmonic coupling. The rotational selection rule is $\Delta J = \Delta K = 0$ between the bright and the dark states. In this case, if a dark state has the same rotational constant as the bright state (type I), the mixing strengths between these states become equal for all J states. This provides the ratios of the excitation probabilities for the $J - 1$, J, and $J + 1$ state in the dark manifold to be equal to those of the bright states, thus maximizing alignment in the dark

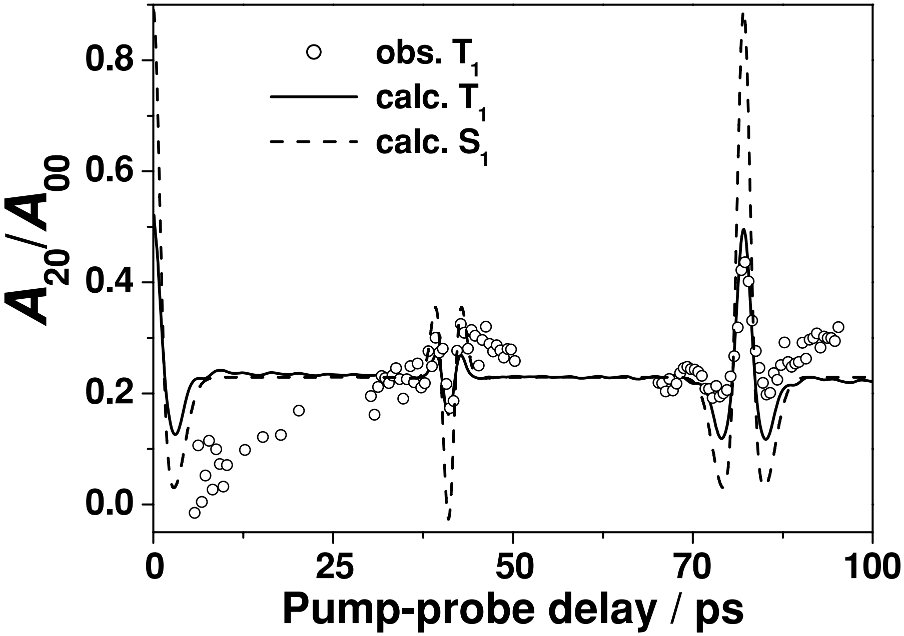

Figure 3 Time evolution of the molecular-axis alignment A_{20}/A_{00}. Open circles represent observed data points for the T_1 state populated via intersystem crossing from the S_1 zero vibrational state. The solid and dashed lines show the calculated time profiles for the T_1 and S_1 states, respectively (see text).

state. On the other hand, if the rotational constants in the bright and dark states differ (type II), the ratios of the excitation probabilities for the $J-1$, J, and $J+1$ state in the dark state deviate from those in the bright state, reducing alignment in the dark state. The case of ISC in pyrazine is different from the intramolecular vibrational–redistribution case because although the rotational constants are essentially the same in the bright and dark states, alignment diminishes in the dark state. The key difference of intersystem crossing from intramolecular vibrational redistribution is that the spin-orbit interaction provides the selection rule ($N = J-1, J, J+1, K = P \pm 1$) that allows three different rotational ladders in T_1 to be involved in the ISC. We term them types A ($N = J$), B ($N = J+1$), and C ($N = J-1$). Type A is analogous to type I of the intramolecular vibrational–redistribution case, whereas types B and C are analogous to type II. The type A scheme provides rotational revival in the dark state with the same strength as the bright state, in contrast with the cases of types B and C. Therefore, types B and C contribute to the sources of reduced alignment in the dark state.

In general, appearance of the rotational wave-packet dynamics in the dark state depends on the ratio between a coupling strength and an energy difference between the bright and dark states. When the coupling strength increases, the rotational

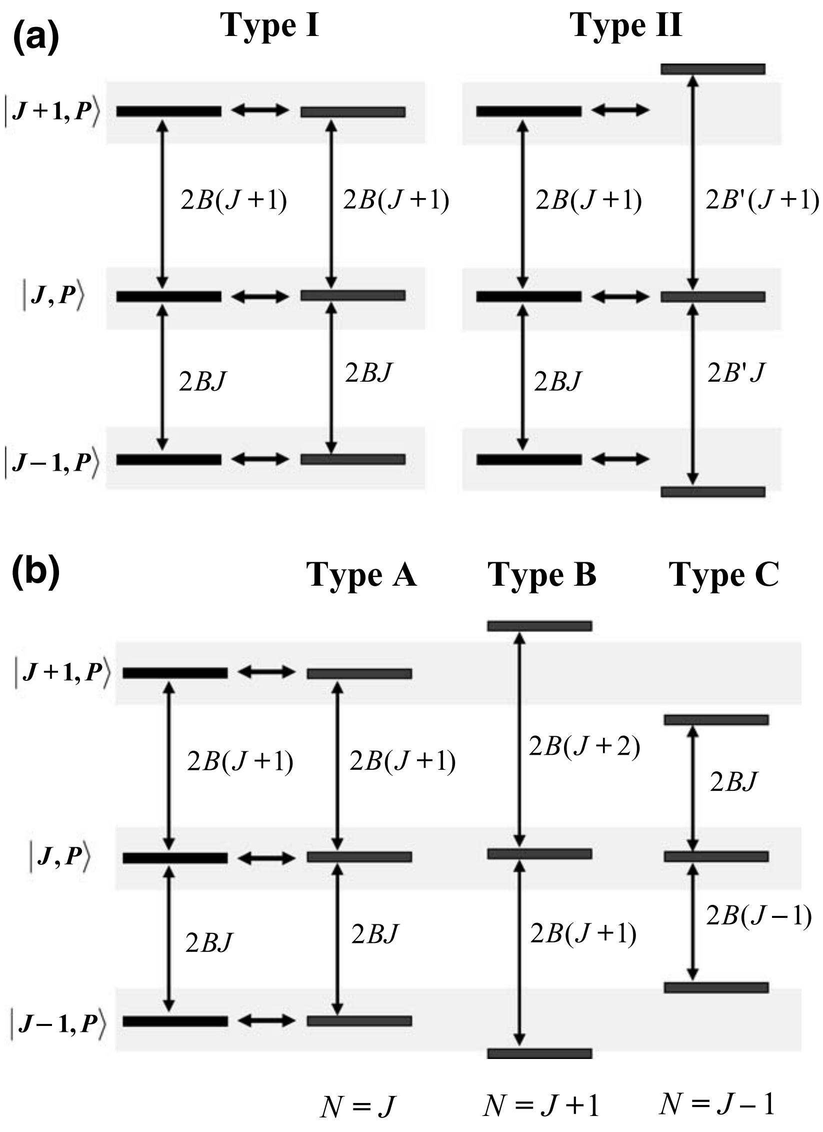

Figure 4 A picture of the rotational energy–level structure of the interacting bright and dark states in the case of (*a*) intramolecular vibrational redistribution and (*b*) intersystem crossing. In type I, the rotational constants of the bright and dark states are the same, whereas they differ in type II. In intersystem crossing, type A, B, and C ladders of the rotational states in the dark state can be coupled with a bright state. Even if the rotational constant in the dark state is the same as that in the bright state, the ladder spacings of types B and C are different from that in the bright state. The shaded area around each bright state indicates the magnitude of the interaction strength with the dark states.

wave-packet revivals in the dark state can appear for larger differences in the rotational constants from the bright state.

PHOTOIONIZATION DYNAMICS VIA TIME-RESOLVED PHOTOELECTRON IMAGING

A rotational wave packet affects LF-PAD primarily because MF-PADs generally differ for different ionization-dipole moments. When LF-PADs are analyzed in detail via Equation 6, TRPEI serves as a means to probe ionization dynamics.

Extraction of Photoionization-Dynamical Parameters from Photoelectron-Angular Distribution

Experimental studies of ionization dynamics ultimately aim at the observation of the MF-PAD expressed by (13, 89–100)

$$\frac{d\sigma}{d\Omega_k} = \sum_{l=0}^{2l_{\max}} \alpha_{lm} Y_{lm}(\theta_k, \phi_k), \qquad 13.$$

where $l_{\max}$ is the largest orbital-angular momentum of the outgoing photoelectron, and θ_k and ϕ_k are the polar and azimuthal angles, respectively, of the photoelectron $\boldsymbol{k}$-vector measured in the MF. Following intricate analysis, the MF-PAD yields photoionization-dynamical parameters such as transition-dipole moments to individual partial waves and the phase shifts. The MF-PAD can be observed by angle-resolved photoelectron-photoion coincidence, which simultaneously observes the velocities of the photoelectron and the daughter ion in dissociative photoionization. From this observation, the angular correlation between the molecular axis and the photoelectron $\boldsymbol{k}$-vector is determined. Reference 101 summarizes recent advances in coincidence techniques. As a result of its nature, photoelectron-photoion coincidence can provide MF-PADs only for dissociative ionization in the axial recoil limit. An alternative approach presented by Zare and coworkers (102–109) was to measure LF-PADs for the state-to-state ionization process with various polarization combinations of the pump and probe lasers, from which ionization-dynamical parameters were extracted.

In TRPEI, time-dependent LF-PAD provides the a_{KL0} parameters via Equation 6, which can be solved, in principle, to obtain the photoionization-dynamical parameters. Here I present an example of $(1 + 1')$ REMPI of NO via the A $(^2\Sigma^+)$ state (110). The NO$^+$ ion has a closed shell with the electron configuration $1\sigma^2 2\sigma^2 3\sigma^2 4\sigma^2 1\pi^4 5\sigma^2$. Nitric oxide is the benchmark system for studies of molecular photoionization (111, 112) and Rydberg states (113–117). It has been the only molecule for which photoionization-dynamical parameters have been determined experimentally (102–109); however, these experiements have only been for PKE $= 0.18$ eV. This fact illustrates the limited understanding of ionization dynamics of molecules near the threshold. Figure 5 shows the overview of the time-dependent anisotropy parameters observed in the $(1 + 1')$ TRPEI of NO via the $v' = 0$ level in the A ($^2\Sigma^+$) state. The data points shown here are from our new measurements performed after the 2004 report (110). In the experiment, a femtosecond 226-nm pump pulse created a rotational wave packet in the A state of NO, and a time-delayed femtosecond probe pulse ionized the molecules from the A state. Because the A state is the 3sσ Rydberg state, the $\Delta v = 0$ propensity rule holds in photoionization, and the PKE associated with the single vibrational state ($v^+ = 0$) of NO$^+$ was continuously varied with the ionization wavelength. The rotational wave-packet revivals are clearly identified in β_2 and β_4, although the time-dependent variations are less than 0.1 at some PKEs (Figure 5). The full revival time of the rotational wave packet is 8.2 ps. Both β_2 and β_4 show a clear trend against PKE: Anisotropy parameters at the full revival time exhibit the minima at the lowest PKE, whereas they exhibit the maxima at the largest PKE. The phase reversal at PKEs of approximately 0.3 eV (β_2) and 0.5 eV (β_4) clearly indicates that the MF-PADs vary with the PKE. Because the molecular axis of NO in the A state is primarily perpendicular to the laser polarization at $t = 0$ and 8.2 ps, ionization at these moments occurs predominantly via the perpendicular transition to create a kπ scattering wave. Conversely, at 4.2 ps, ionization mainly occurs via the parallel transition to the kσ ionization continuum. Therefore, Figure 5 indicates that MF-PAD exhibits a sharper peak for the σ-ionization channel than for the π channel near the threshold, whereas this relation is reversed at PKE > 0.5 eV.

Because an electron wave function of a molecule is referenced to the MF, the one-electron scattering wave in the LF is expressed as

$$|\psi^-(\vec{k}', \vec{r}'; R)\rangle = \sum_{lm\lambda} i^l e^{-i\sigma_l} Y^*_{lm}(\hat{k}') D^{l*}_{m\lambda}(\hat{R}) \varphi_{l\lambda}(\vec{r}; k, R), \qquad 14.$$

where variables with and without the prime correspond to the LF and MF, respectively. $\vec{k}' = k\hat{k}'$ is a wave vector of the photoelectron with $\hat{k}'$ as the unit vector along the direction of ejection, and $\vec{r}' = r\hat{r}'$ is a similar relation for the position of the photoelectron; l is the orbital angular momentum, and m is its projection quantum number onto the LF z-axis, σ_l is the Coulomb phase shift of a partial wave with l, R is the internuclear distance, and $\hat{R}$ is the Euler angle that relates the MF to LF. As the orbital-angular momentum l is not a good quantum number for molecules, the partial waves $\varphi_{l\lambda}(\vec{r}; k, R)$ are generally not the eigenfunctions. Because mixing between the sσ and dσ Rydberg orbitals (s,d supercomplexes) have been identified for NO by extensive spectroscopic and theoretical analyses (113–115), similar mixing is anticipated for the sσ and dσ scattering waves. The origin of this mixing has been speculated to be a result of interactions with the HOMO(5σ) of NO$^+$, which has a mixed sσ + dσ character. To account for this s-d mixing, Park & Zare (108, 109) employed the electronic eigenchannel wave functions $\xi^\lambda_{i_\lambda}(\vec{r}; k, R)$ composed of partial waves with the same λ. Each partial wave in Equation 14 is then expressed by

$$\varphi_{l\lambda}(\vec{r}; k, R) = \sum_{i_\lambda} U^\lambda_{li_\lambda} \exp\left(-i\pi\tau^\lambda_{i_\lambda}\right) \xi^\lambda_{i_\lambda}(\vec{r}; k, R), \qquad 15.$$

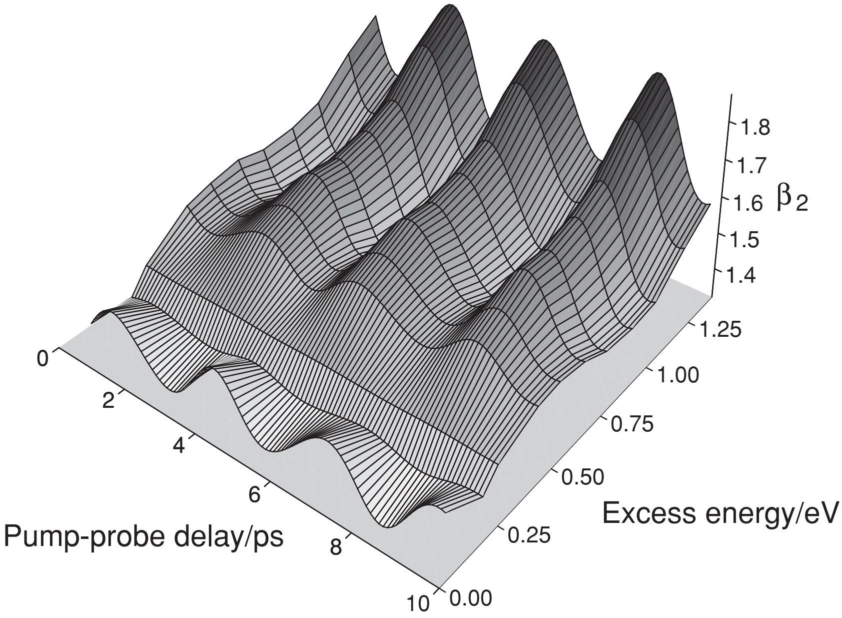

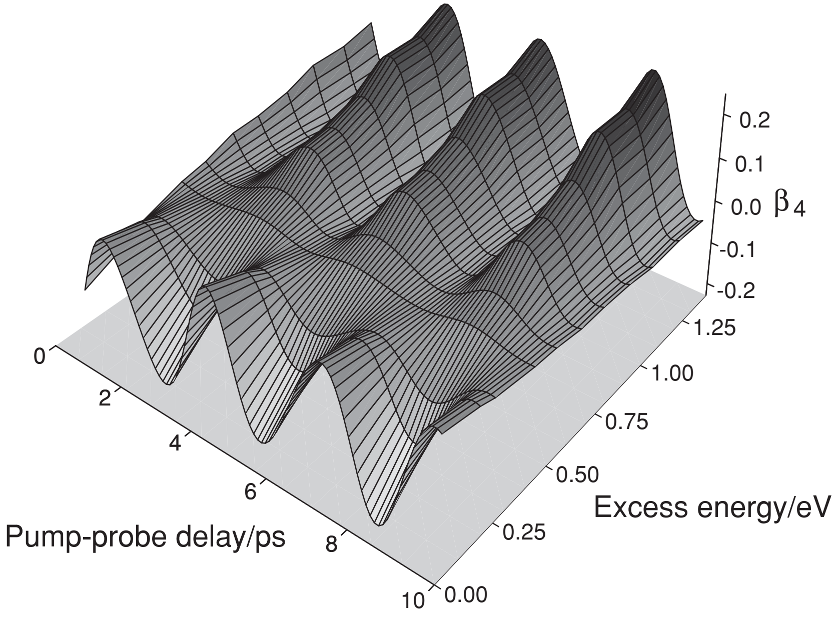

Figure 5 Experimentally observed variation of the photoelectron-anisotropy parameters β_2 and β_4 as functions of the pump-probe time delay and the probe wavelength in one-photon ionization from the A state $v' = 0$ level of NO. $\beta_L = \sqrt{2L+1}\beta_{L0}$.

where $\tau_{i_\lambda}^{\lambda}$ is the dynamical phase shift due to the interaction of an electron with the ion core in the short range, and $U_{li_\lambda}^{\lambda}$ is an element of the transformation matrix that diagonalizes the scattering K matrix (109, 114). The running index i_λ is for numbering the eigenchannel wave functions with the same λ. Considerable configuration mixing occurs only for the sσ and dσ waves in NO.

When the scattering wave function is described by Equations 14 and 15, the a_{KL0} coefficients for $\mathrm{NO}^+ X(^1\Sigma^+) \leftarrow \mathrm{NO} A(^2\Sigma^+)$ are expressed as follows (110):

$$
\begin{aligned}
a_{KL0} \propto{}& \sqrt{(2L+1)(2K+1)} \sum_{P} (2P+1) \begin{pmatrix} 1 & 1 & P \\ 0 & 0 & 0 \end{pmatrix} \begin{pmatrix} P & K & L \\ 0 & 0 & 0 \end{pmatrix} \\
&\times \sum_{l\lambda l'\lambda'} \sqrt{(2l+1)(2l'+1)} \begin{pmatrix} 1 & 1 & P \\ \lambda & -\lambda' & \lambda'-\lambda \end{pmatrix} \begin{pmatrix} P & K & L \\ \lambda-\lambda' & 0 & \lambda'-\lambda \end{pmatrix} \\
&\times \begin{pmatrix} l & l' & L \\ 0 & 0 & 0 \end{pmatrix} \begin{pmatrix} l & l' & L \\ \lambda & -\lambda' & \lambda'-\lambda \end{pmatrix}, \\
&\times (-i)^{l-l'} e^{i(\sigma_i - \sigma_{l'})} \sum_{i_\lambda i'_{\lambda}} U_{i_\lambda}^{\lambda} U_{i'_{\lambda'}}^{\lambda'} M_{i_\lambda}^{\lambda} M_{i'_{\lambda'}}^{\lambda'} \exp\left\{ i\pi \left(\tau_{i_\lambda}^{\lambda} - \tau_{i'_{\lambda'}}^{\lambda'} \right) \right\},
\end{aligned}
\qquad 16.
$$

where $M_{i_\lambda}^{\lambda} = \langle \Psi^+; \xi_{i_\lambda}^{\lambda}(k_M, \vec{r}) | \mu_\lambda | \Psi_{3s} \rangle$ is the magnitude of the matrix element of the ionization transition–dipole moment. Because the ionized orbital is 3sσ ($\lambda = 0$), partial waves are restricted to the σ ($\lambda = 0$) and the π wave ($\lambda = \pm 1$). In addition, because the s character of this orbital is as high as 94.0% (111), the contribution of high angular momentum ($l > 3$) to partial waves is neglected, which is supported by the fact that Zare and coworkers have not detected $\Delta N \geq 4$ transitions in the state-to-state ionization from the A state to the cation (102–109). With these restrictions, there still remain 7 partial waves with 12 dynamical parameters (4 transition-dipole moments and 3 relative phase-shift differences for the σ wave, 3 transition-dipole moments and 2 relative phase-shift differences for the π waves) to account for in the analysis, other than the matrix $U_{l,i_\lambda}^{\lambda}$. On the other hand, the a_{KL0} parameters determinable in the $(1 + 1')$ REMPI are only 4, i.e., relative values of a_{000}, a_{020}, a_{200}, a_{220}, and a_{240}, at each ionization wavelength. Therefore, extraction of the dynamical parameters from TRPEI is not possible from a measurement performed at a single ionization wavelength.

However, as anticipated from the smooth energy dependence of the anisotropy parameters shown in Figure 5, the a_{KL0} parameters determined from these experimental data also vary monotonically with the PKE. This fact suggests that the dynamical parameters can be approximated to vary linearly with PKE. Explicit assumption of this fact facilitates the analysis because the a_{KL0} parameters at each PKE can be employed altogether to determine the dynamical parameters and their first derivatives against the PKE at the ionization threshold. Furthermore, the dynamical phase shift at low energies connects smoothly to the quantum defect of a high Rydberg state through the Levinson-Seaton theorem (118–122).

Therefore, the dynamical phase shifts of the partial waves were estimated by extrapolating the quantum defects in high Rydberg states of NO, and they were excluded from the least-squares fitting. Similarly, $U^{\lambda}_{l,i_\lambda}$ were taken from the results for Rydberg states (113–115). In this way, the energy-dependent transition-dipole strengths for each partial wave $M^{\lambda}_{i_\lambda}(E)$ were determined from the a_{KL0} parameters (110).

Nonlinear least-squares fitting of the second-order Equation 16 generally provides multiple numerical solutions. This is similar to the multiple solutions always encountered in the extraction of dynamical parameters from MF-PAD observed by photoelectron-photoion coincidence (123, 124). However, all the obtained solutions exhibited a major contribution of the p wave; this is in agreement with the $\Delta l = \pm 1$ propensity rule in ionization from the 3sσ state. The MF-PADs calculated from the different sets of dynamical parameters are similar to each other, thus only one example is shown in Figure 6.

In 2004, Guérout et al. (116, 117) reported the ab initio multichannel quantum-defect theory to calculate electronic wave functions of highly excited Rydberg states and the continuum. Further experimental and theoretical investigations are necessary to elucidate the ionization dynamics of this benchmark system, and they should be extended to other molecules.

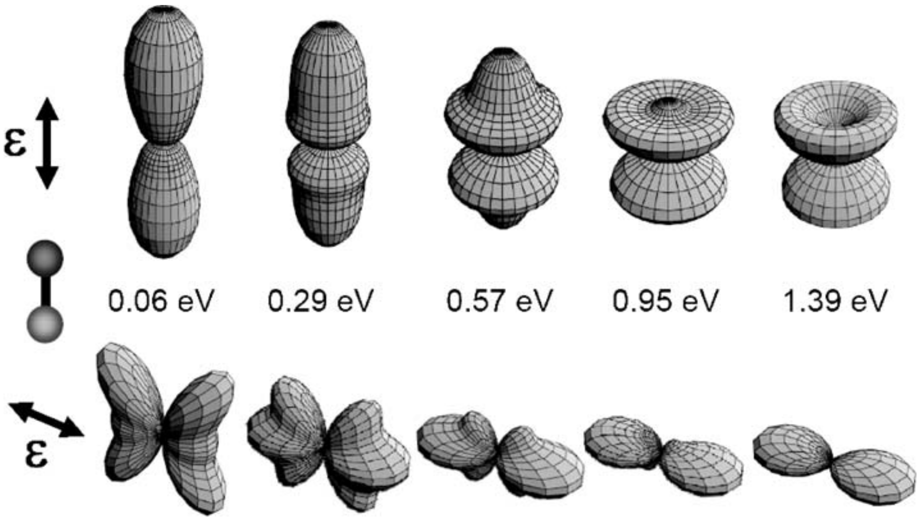

Figure 6 Molecular-frame photoelectron-angular distributions in one-photon ionization of NO from the A state $v' = 0$ level calculated using one set of $M^{\lambda}_{i_\lambda}(E)$ determined by the least-squares fitting of Equation 16. The dynamical phase shifts $\tau^{\lambda}_{i_\lambda}$ were estimated from the quantum defects in high Rydberg states. The matrix elements of $U^{\lambda}_{l,i_\lambda}$ to describe the sσ-dσ mixing were taken from those for high Rydbeg states. See the text for details.

Strategies for Narrower Axis Distribution

If a strongly aligned ensemble of molecules is prepared prior to photoionization, LF-PAD will be identical to MF-PAD. However, such strong alignment cannot be created by one-photon excitation because the unit spin–angular momentum of a photon restricts the rotational wave-packet components to only the $J - 1$, J, and $J + 1$ eigenstates. This leads to a molecular-axis distribution of $\cos^2\theta'_z$ or $\sin^2\theta'_z$ at most. Because of the uncertainty principle, a narrower axis distribution requires the superposition of a large number of J states. A pendular state of a polar molecule in a static electric field (125–127) or a polarizable molecule in a (quasi-)stationary laser field (128–131) is also a way of achieving alignment or orientation; however, the presence of strong external fields is inconvenient for photoelectron spectroscopy. The employment of an intense laser field is considered to be a more promising method. Interaction of an intense laser pulse with a molecule induces rapid Rabi-cycling in which rotational ladder climbing and superposition of a broad J distribution occur (132). In addition, when the laser turn-on and turn-off times are considerably shorter than the rotational time period, the rotational dynamics are nonadiabatic in that a rotational wave packet persists even after the alignment laser field vanishes, thus providing field-free molecular-axis alignment. Although a wave packet can be created via resonant and nonresonant interaction of a laser field with a molecule (132), the latter can be implemented more easily with an amplified titanium sapphire laser (800 nm) (133). The nonresonant scheme is essentially multiple rotational–Raman scattering (134).

As an example, Figure 7 shows a calculated molecular-axis distribution of N_2 in the ground-electronic state after interaction with a nonresonant-femtosecond laser pulse (800 nm) (135). The distribution becomes narrow at particular time delays. Dooley et al. have verified the time-dependent axis distributions of N_2 and O_2 created by multielectron-dissociative ionization and imaging of the daughter-ion recoil directions (136). Figure 8 shows the observed alignment moment $\langle\cos^2\theta'_z\rangle$ and the axis distributions measured at specified time delays. The LF-PAD measurement using such transient molecular axis alignment has not yet been realized: Only a theoretical prediction has been reported for the LF-PADs from the aligned N_2 molecules for the $2\sigma_g$-shell photoionization ($h\nu = 58.2$ eV) and (2 + 1) REMPI via the $a''(^1\Sigma_g^+)$ state at 205 nm (135). The calculated LF-PAD clearly exhibited a characteristic nodal pattern of the MF-PAD when ionized at the maximal axis alignment.

In general, a single pulse–alignment scheme meets saturation when the alignment is no longer enhanced by the laser intensity. For squeezing the axis distribution beyond the saturation limit, employment of multiple laser pulses has been proposed (137–139). In the multiple-pulse schemes, the first pulse creates transient alignment of the molecular axis in the harmonic region of the angular-interaction potential ($\sin\theta \approx \theta$), where the subsequent pulse provides the angular velocity ($\omega \propto \sin\theta$) linearly proportional to the angle between the molecular axis and the

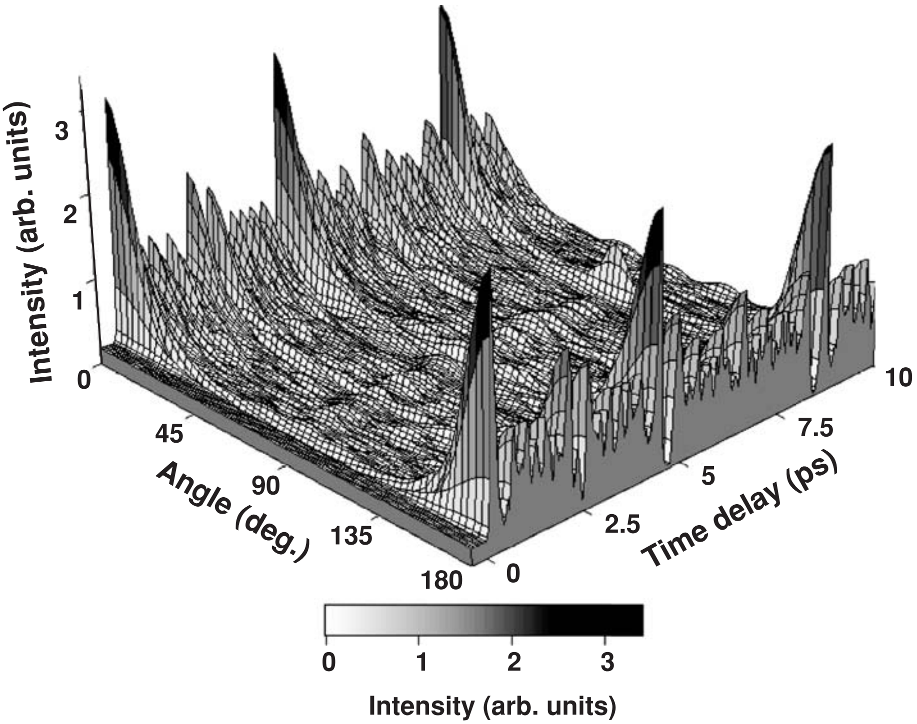

Figure 7 Calculated time-dependent molecular-axis distribution in the ground state of N_2 created by interaction with an intense laser field. The initial rotational temperature was assumed to be 20 K. The intensity and pulse width of the alignment-laser light in the calculation are $I = 100$ TW/cm^2 and $\Delta t_{align} = 100$ fs, respectively.

laser polarization, thereby squeezing the angular distribution. The suggested enhanced alignment by the two-pulse scheme has been experimentally observed (140, 141). These calculations and experiments were performed for linear molecules.

In the case of asymmetric top molecules, maximal alignment occurs initially because complex rotational energy structures prevent the complete revival of the initially aligned state. Péronne et al. (142) aligned iodobenzene with a 2.2-ps-long alignment pulse and observed strong alignment at a time delay of approximately 2 ps. Asymmetric top molecules provide another interesting problem of the field-free 3D alignment of molecules, for which several strategies have been proposed (143–145).

For application of MF-PAD measurements by TRPEI considered here, it is important to precisely characterize the axis distribution created by a laser pulse prior to LF-PAD measurement. The creation of a strongly aligned molecular ensemble without contamination from weakly aligned molecules is more difficult than the observation of the revival features on top of a background. In the weak-field

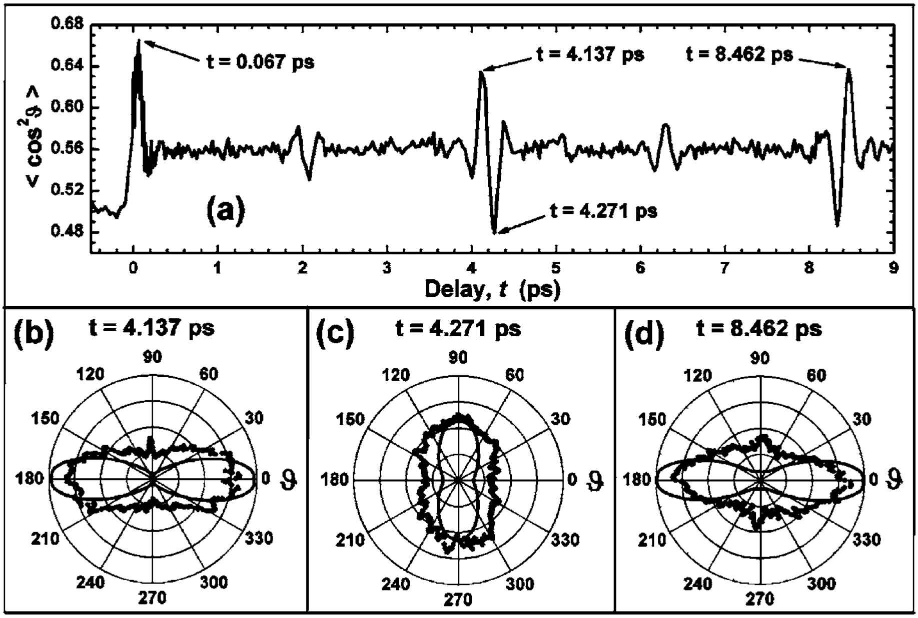

Figure 8 (*a*) Variation of the molecular-axis alignment moment $\langle \cos^2\theta \rangle$ of N_2 with a time delay between the alignment and explosion (dissociative-ionization) pulse. Prior to the alignment pulse, the molecular ensemble of N_2 is isotropic. (*b–d*) Plots of measured (*dots*) and simulated (*lines*) N_2-axis distributions. Polarization of the alignment pulse is in the horizontal direction; anti-alignment is seen at the half revival time in panel c. For clarity, the areas of the simulated plots are two-thirds those of the measured distributions.

case discussed in the above section, the alignment is mild but is completely characterized (and predictable). Molecular-axis alignment also attracts attention in laser physics as it can be used for quasi-phase matching in high-harmonic generation and attosecond pulse shaping (146).

IONIZATION CONTINUA OF POLYATOMICS: POORLY UNDERSTOOD FINAL STATE

In TRPEI, if the final state for ionization, rovibronic wave functions of a cation and photoelectron-scattering waves, were well understood, the ionization continuum would serve as an ideal screen to project complex dynamics in the neutral state. In reality, the rovibronic states of cations are poorly understood, especially those of large molecules that exhibit interesting dynamics, and virtually nothing is known about electron-scattering wave functions. The latter is particularly problematic for interpretation of the absolute values of anisotropy parameters and is briefly discussed in this section.

Using conventional photoelectron spectroscopy, a number of mechanisms have been elucidated as origins for energy-dependent photoelectron-angular anisotropy $\beta(E)$: (*a*) For instance, in photoionization from the inner p subshells of rare gases (Ar 2p, Kr 3p, and Xe 3p and 4p), anisotropy parameters vary with the ionization energy due to the Coulomb phase shifts of the s and d partial waves (147). $\beta(E)$ drops sharply with an excess energy above the ionization threshold and then increases smoothly to reach an asymptotic value of approximately 1.5. (*b*) Interaction of the ionization continuum with superexcited states exhibits resonances, such as the Beutler-Fano type, and provides a $\beta(E)$ that varies sharply around the energy of the superexcited state (12). (*c*) Photoionization from the subshells of $l < n - 1$ exhibits the Cooper minimum in that a transition-dipole moment to a particular partial wave vanishes at a certain energy; $\beta(E)$ varies in a wide energy range (14). The Cooper minimum observed in molecular photoionization is generally ascribed to the atomic character of the molecular orbital, in which the effect is much less pronounced than in the atomic case. (*d*) In molecular photoioinzation, the PAD is affected by shape resonance due to excitation to an unoccupied molecular orbital that rapidly decays into the continuum (148).

Photoionization from various orbitals exhibits a characteristic $\beta(E)$. Piancastelli et al. (149) have assigned the π^{-1} and n^{-1} bands in photoelectron spectra of azabenzenes based on the experimental evidence that π^{-1} generally exhibits a $\beta(E)$ that increases with excess energy, whereas n^{-1} shows a much lower anisotropy and weak energy dependence. We have examined this phenomenon using continuum-multiple scattering (CMS)-Xα calculations (150, 151). Figure 9 shows the calculated $\beta(E)$ for ionization of π electrons in benzene, pyridine, and pyrazine. The molecules are assumed to be randomly oriented. The experimental values (149, 152) (filled circles and triangles) and calculations (solid and dotted lines) are in excellent agreement. The smooth variation with excess energy seen in all cases is a result of the energy-dependent Coulomb phase shifts of the partial waves. Conversely, photoionization of the σ and n electrons exhibits completely different features (Figure 10). The circles and diamonds represent the experimental $\beta(E)$ values (149, 152, 153). The calculated $\beta(E)$ for ionization from the $3e_{1u}(\sigma)$ orbital in benzene are in reasonable agreement with the experimental result, which is the same as that obtained by Carlson et al. (153). The partial cross section to the ke_{2g}, ka_{1g}, and ka_{2g} continua is also shown in the same panel. The enhanced cross sections around 6 eV and 12 eV indicate the shape resonances with the $a_{2g}(\sigma)$, $a_{1g}(\sigma)$, and $e_{2g}(\sigma)$ unoccupied orbitals. A close comparison of the anisotropy parameter and the cross section reveals that $\beta(E)$ is indeed influenced by shape resonances. The result of the pyridine $6b_2(\sigma)$ orbital that correlates with the benzene $3e_{1u}$ one is similar. For pyrazine, calculations are shown for $4b_{2u}(\sigma)$ and $5b_{1u}(n)$. Again, $\beta(E)$ is determined by shape resonances. A close examination of Figure 9 reveals the effect of shape resonance on the σ^* orbital in ionization from π as dips in the curves; however, this effect is negligible. These results support the argument by Piancastelli et al. (149) and illustrate that the shape resonance is a crucial factor in determining the PAD, particularly in ionization from the nonbonding and σ orbitals.

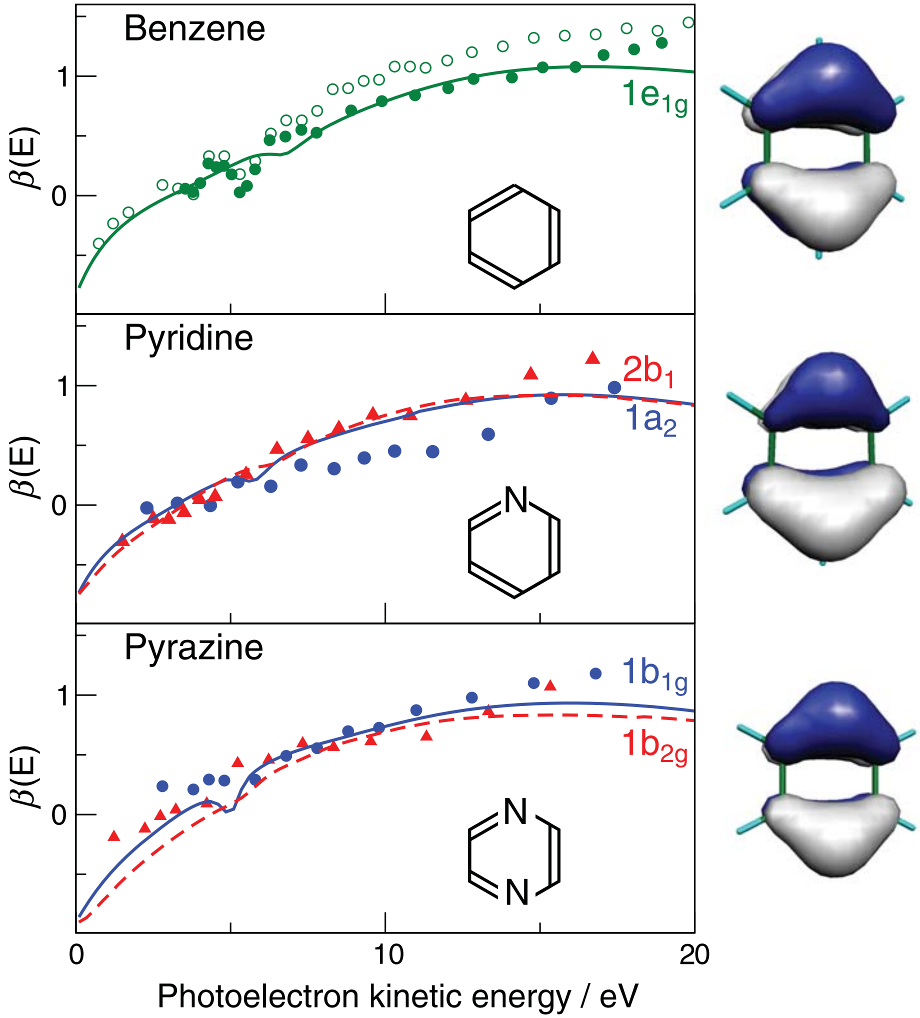

Figure 9 (*left*) Photoelectron-anisotropy parameter as a function of photoelectron kinetic energy calculated for orbitals $1e_{1g}$ of benzene, $1a_2$ (*solid line*) and $2b_1$ (*dashed line*) of pyridine, and $1b_{1g}$ (*solid line*) and $1b_{2g}$ (*dashed line*) of pyrazine. Experimental data are indicated by open circles (153) and filled circles for benzene (152), and filled circles and triangles for pyridine (pyrazine) $1a_2$ ($1b_{1g}$) and $2b_1$ ($1b_{2g}$), respectively (149). (*right*) Isosurfaces of HF/4-31G molecular orbitals. Benzene $1e_{1g}(xz)$, pyridine $1a_2$, and pyrazine $1b_{1g}$ orbitals are shown.

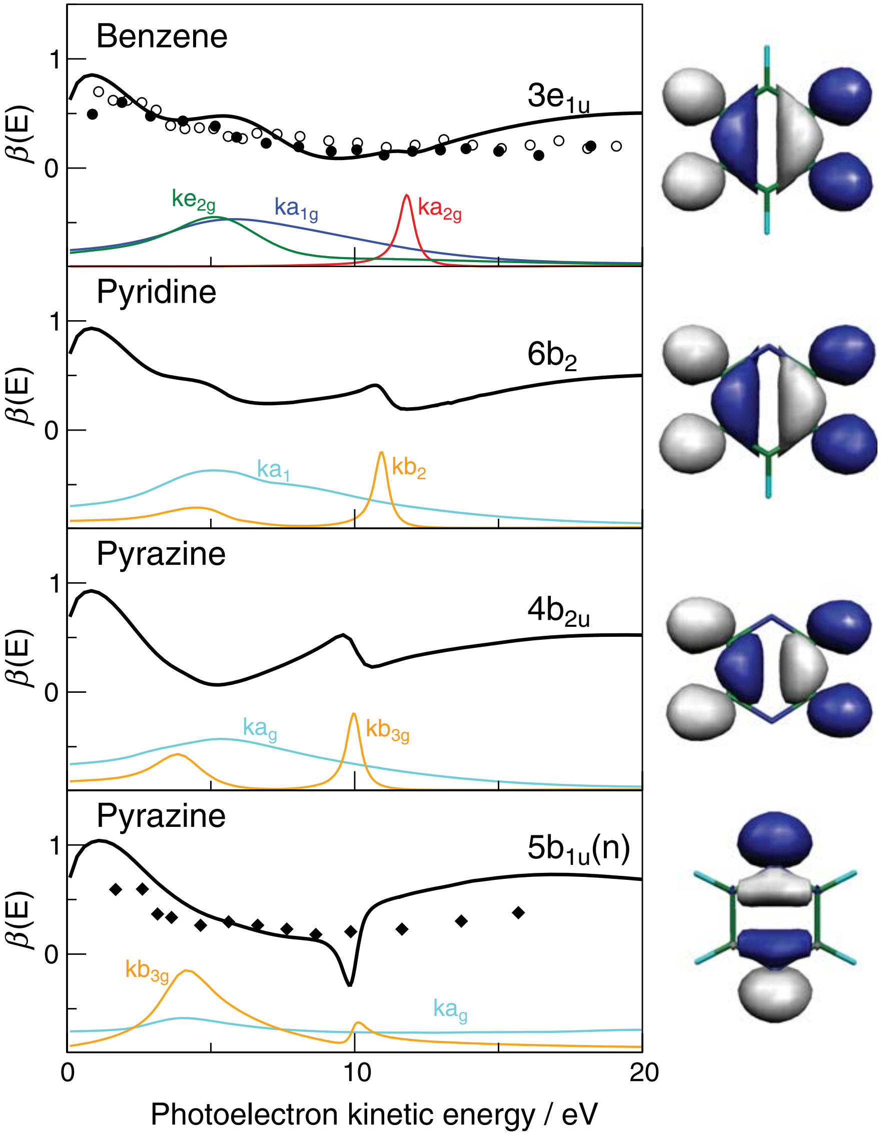

Figure 10 (*left*) Photoelectron-anisotropy parameter as a function of photoelectron kinetic energy calculated for the orbitals, benzene $3e_{1u}$, pyridine $6b_2$, and pyrazine $4b_{2u}$ and $5b_{1u}$. Experimental data are shown by open circles (153), filled circles (152), and diamonds (149). Partial cross sections are plotted for benzene using green (ke_{2g}, C = C*), blue (ka_{1g}, C-H*), and red lines (ka_{2g}, C = C*), respectively. For pyridine and pyrazine, cyan lines indicate partial cross sections for the waves correlated with the benzene $ke_{2g}(x^2 - y^2)$ and ka_{1g} that are no longer separable in lower symmetry. Orange lines are for the waves correlated with the benzene $ke_{2g}(xy)$ and ka_g waves. (*right*) Isosurfaces of ionized molecular orbitals calculated at the level of HF/4-31G.

Bellm & Reid (154) observed the photoelectron anisotropy parameter that varies with the PKE in nanosecond $(1 + 1')$ REMPI of jet-cooled paradifluorobenzene via the S_1 (B_{2u}) state; β_{20}/β_{00} diminished from 0.5 to -0.2 within PKE < 1 eV. In 2005, Bellm et al. (155) reported CMS-Xα calculations that qualitatively reproduced the gradual depression of the anisotropy parameter in the first 1 eV above the threshold. The energy dependence was attributed to a $k\mathrm{b}_{2g}$ shape resonance centered at PKE $=$ 2 eV. The calculations predict that the anisotropy parameter increases again in PKE $>$ 3 eV, which, however, has not been experimentally confirmed. As for the region of PKE $<$ 1 eV, several notable disagreements remain between the experiment and the theory. The observed PAD was insensitive to the alignment in S_1, whereas calculations predicted an alignment dependence. Furthermore, the experimental PADs best agreed with those predicted by CMS-Xα, when ionization is assumed to occur from the maximally aligned ensemble of molecules in the S_1 state contradicting the experimental conditions when using nanosecond lasers. It is also interesting that the observed photoelectron spectra exhibited no variation of the vibrational structure with the excess energy, whereas shape resonances in other systems normally provide it. These interesting features should be explored further both experimentally and theoretically. Although Bellm et al. (155) have employed a time-of-flight photoelectron spectrometer, similar measurements could be carried out more easily using a photoelectron imaging method.

Theoretical calculations of PAD using the random-phase approximation (156), the Schwinger variational method (157), and the R-matrix method (158) are more accurate than using CMS-Xα. However, these methods are computationally demanding, and applications to large molecules are scarce (159). Time-dependent density functional theory (160, 161) is a promising approaches to large systems. Further development of theoretical methods sufficiently accurate for large polyatomic molecules, especially those to examine ionization from the excited states, is of great importance for TRPEI.

Photoelectron-angular anisotropy in photodetachment of anions is generally more easily interpreted than the neutral case. Sanov and coworkers (162, 163) have studied energy dependence of photoelectron-angular anisotropy in photodetachment of solvated atomic anions. They analyzed the PAD using a Cooper-Zare formula (164, 165) analogously with the works on bare atomic anion (166, 167). As the Coulomb phase shift is absent in photodetachment of anions, the phase-shift difference between the two partial waves is fixed over the excess energy. The photoelectron anisotropy is influenced by the ratio of the two transition dipoles to the $l + 1$ and $l - 1$ outgoing waves, and these tend to vary linearly with the excess energy, as predicted by Wigner's threshold law (168). The observed trend of $\beta(E)$ was reproduced fairly well by the Cooper-Zare formula.

LONG-RANGE INTERACTION AND INTERFERENCE

Photodissociation of I_2^- has been studied in detail using TRPES (169, 170). Photoexcitation of I_2^- at approximately 800 nm creates a wave packet on the dissociative $^2\Pi_{g,1/2}$ potential curve, which rapidly moves toward the asymptote of I $(^2P_{3/2})$ and

I^- ($^1S_0$). The wave-packet motion from the molecular to the atomic region is almost completed within the first 200 fs, which is represented by the PKED that narrows down to an atomic line of I^-. Within 300–600 fs, the wave packet travels through a shallow basin (0.0017 eV) due to the charge-induced dipole interactions between I($^2P_{3/2}$) and I^-, centered at an internuclear distance of 6.2 Å, which results in a slight reverse shift in the PKED. In the subsequent range of 600–3000 fs, the bond length increases further from approximately 10 Å to 40 Å, during which no further change in the PKED is discernible. In 2003, Davis et al. (171) reexamined this system by TRPEI using pump- and probe-laser wavelengths of 793 nm and 265 nm, respectively, and found an interesting feature of PAD. The anisotropy parameter β_2 initially decreased from approximately −0.1 near $t = 0$ to −0.55 near $t = 200$ fs, as a result of the wave-packet motion from the molecular (I_2^-) to the atomic (I^-) region; however, the β_2 value increased to −0.44 near 580 fs and declined again after 800 fs. Davis et al. (171) ascribed the increase of β_2 to the wave-packet motion from the shallow basin, whereas they attributed the slight decrease after 800 fs to the process in which an electron distribution changes from a delocalized one with the same amplitude on each I atom to a localized one at an iodine atom due to the *gerade*/*ungerade* mixing between the $^2\Pi_{g,1/2}$ and $^2\Sigma_u^+$ state induced by hyperfine coupling or an external field. In 2005, Mabbs et al. (172) repeated the same experiment with slightly different wavelengths of the pump (780 nm) and probe (390 nm) lasers. They observed that the β_2 parameter varied from approximately −0.2 at $t = 0$ to −0.36 at 1.5 ps, and it increased to −0.17 at approximately 3 ps. Such a variation was not observed for IBr^-, indicating that this phenomenon is related to the nature of homonuclear diatomic molecules. Mabbs et al. (172) interpreted the time dependence of β_2 as the interference in a photodetached electron from two equivalent sites in the homonuclear diatomic molecule I_2^-. The difference in the timescale of the variation in the β_2 parameter between Davis et al. and Mabbs et al. was ascribed to the different de Broglie wavelengths of photoelectrons—10 Å in the former and 35 Å in the latter. A quantitative analysis yielded the best agreement with the experiment performed by Mabbs et al. when the de Broglie wavelength was assumed to be 43 Å. Although further theoretical analysis seems necessary for completely elucidating the physics behind time-dependent anisotropy, these works demonstrated that the PAD can serve as a sensitive probe for understanding the dynamics in regions where the PKED no longer provides useful information.

TOWARD DYNAMICS IN THE CONDENSED PHASE

Liquid electron spectroscopy for chemical analysis pioneered by K. Siegbahn, H. Siegbahn, and coworkers (173, 174) has been extended more recently by Faubel et al. (175–181). Because the mean free path of an electron in the bulk is generally short, especially at low energies, photoelectron spectroscopy is essentially a surface-sensitive method. However, if nanoscale aggregates that mimic the bulk properties are targeted, TRPEI in the gas phase may become a powerful tool in disentangling complex dynamics in the condensed phase.

In 2004, Neumark et al. (21, 22) applied TRPEI to large water-cluster anions. The hydrated electron in the condensed phase is a trapped electron in the cavity defined by six OH bonds in bulk water. Its property may be regarded as analogous to a color center or a quantum dot in the solid phase; however, a hydrated electron experiences a considerably more flexible environment. Consequently, photoexcitation of a hydrated electron from the ground-state s orbital to an excited p orbital may induce reorganization of a solvation shell upon a sudden change of the electron cloud. Alternatively, it might lead to an ultrafast internal conversion down to the s state as a result of a strong interaction between the p and s states. Thus, photophysics of a hydrated electron has been controversial (182–188). Figure 11 shows the TRPEI of $(D_2O)_{25}^-$. A pump pulse at 1250 nm excites a hydrated electron from the s state to the p state, and the probe pulse at 400 nm detaches the electron.

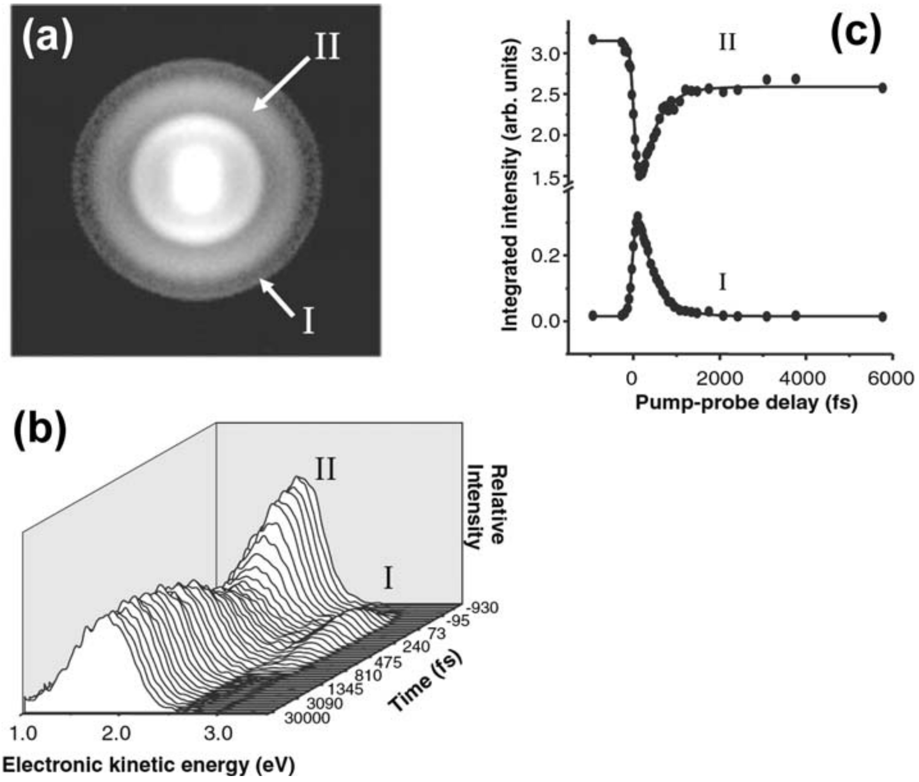

Figure 11 Time-resolved photoelectron imaging of water cluster anions. (*a*) Photoelectron image of $(D_2O)_{25}^-$ collected at the 1250 nm + 400 nm pump-probe temporal overlap. Features I and II arise from the two-color resonant and direct 400-nm photodetachment processes. (*b*) Time-resolved photoelectron spectra of $(D_2O)_{25}^-$. Features highlighted in part a are displayed with the corresponding pump-probe delays. (*c*) Integrated intensities of features I and II versus pulse delay (*circles* represent experiment; *lines* represent fit). The fit curves produce a 398 ± 50-fs electronic lifetime for the excited cluster.

Figure 11*a* is the photoelectron image observed at t = 0, in which a two-color signal appears as a thin outermost ring denoted as I. The direct photodetachment from the ground state by the probe pulse results in a broader distribution denoted as II. Figure 11*b* shows the time evolution of the signals I and II that represent the population in the p and s states, respectively. The integrated intensities of the features I and II are also plotted (Figure 11*c*), in which the decay of the p state and the recovery of the s state exhibit the identical time constant (21). When the time constant measured for various cluster sizes were extrapolated to the bulk, it agreed quite well with the time constant, approximately 50 fs, observed for the dynamics immediately after the photoexcitation of a hydrated electron in bulk water. Paik et al. (189) have drawn similar conclusions. Neumark and coworkers (22) have also addressed whether an excess electron in the anion thus observed is indeed inside the cluster or on the surface. They found one species with a long lifetime in the p state and weak dependence of the vertical detachment energy on the cluster size under the molecular beam conditions where the clusters have a low temperature. Conversely, the conditions for higher temperatures provided another species with much shorter lifetimes and larger vertical detachment energies that varied more strongly with the cluster size. The former species was assigned to a surface electron on an ice nanocrystal whereas the latter was assigned to the hydrated electron in the cluster. It was confirmed that their earlier TRPEI experiment was indeed for an internal state, thereby strongly suggesting that the ultrafast dynamics in a photoexcited hydrated electron in the p state is a direct internal conversion to the s state. Conversely, interpretation of the observed PADs has not been reported and it awaits future work.

BRIEF SUMMARY AND OUTLOOK

This review presents general aspects of TRPEI and time-dependent photoionization DCSs in application to the studies of wave-packet dynamics, electronic dephasing, and photoionization dynamics. Molecular-axis alignment in perturbative and nonperturbative regimes is also described. Although discussion on ultrafast-laser technology is omitted, it is essential for successful TRPEI experiments and coherent control. Whereas pyrazine and NO were the first systems studied by TRPEI using a 10-Hz ultrafast-laser system in 1998 (17), extensive and efficient measurements for obtaining detailed information were made possible by a stable 1-kHz laser system with optical parametric amplifiers to generate tunable pump- and probe-laser pulses.

Future efforts include a better understanding of the ionization continuum for large polyatomic molecules that exhibit interesting photoinduced dynamics. For quantitative analysis of time-dependent photoionization DCSs, development of theoretical methods to calculate continuum wave functions of polyatomic molecules is crucial. Such theoretical efforts need assistance from detailed experimental studies on photoionization dynamics. Only a few experimental studies have been conducted on molecular photoionization dynamics near the ionization threshold at the level of photoionization-dynamical parameters, and further studies with TRPEI and other experimental methods are indispensable for elucidation of ionization dynamics. TRPEI experiments will be revolutionized by development of a particle detector that registers the arrival positions and arrival times for tens of electrons in a short response time. Creation of strongly aligned or oriented molecular ensemble will be useful for studying stereodynamics of photoinduced reactions and photoionization, although the rotational degrees of freedom cannot always be decoupled from vibronic dynamics. Sharpness will not be the most important characteristic of the axis distribution; the homogenuity and precise characterization of the distrbution determine the quality of information extracted for photoionization. Linear and nonlinear excitation processes of a molecule can create superposition of multiple vibronic states with different rotational dynamics, which may create interesting interferences in the TRPEI observables.

ACKNOWLEDGMENTS

Financial support from the Ministry of Education, Culture, Sports, Science, and Technology of Japan and the Japan Science and Technology Agency are gratefully acknowledged. I am indebted to M. Tsubouchi and Y. Suzuki for their contributions to the experimental and theoretical studies on TRPEI at RIKEN.

The *Annual Review of Physical Chemistry* is online at
http://physchem.annualreviews.org

LITERATURE CITED

1. Taylor EH, Datz S. 1955. Study of chemical reaction mechanisms with molecular beams. The reaction of K with HBr. *J. Chem. Phys.* 23:1711–18
2. Lee YT, MacDonald JD, LeBreton PR, Hershbach DR. 1969. Molecular beam reactive scattering apparatus with electron bombardment detector. *Rev. Sci. Instrum.* 40:1402–8
3. Shiu W, Lin JJ, Liu K. 2004. Reactive resonance in a polyatomic reaction. *Phys. Rev. Lett.* 92:103201
4. Zhou J, Lin JJ, Liu K. 2004. Observation of a reactive resonance in the integral cross section of a six-atom reaction: F + CHD_3. *J. Chem. Phys.* 121:813–18
5. Zhang B, Liu K. 2005. Imaging a reactive resonance in the Cl + CH_4 reaction. *J. Chem. Phys.* 122:101102
6. Casavecchia P. 2000. Chemical reaction dynamics with molecular beams. *Rep. Prog. Phys.* 63:355–414
7. Liu K. 2001. Crossed-beam studies of neutral reactions: state-specific differential cross sections. *Annu. Rev. Phys. Chem.* 52:139–64
8. Skodje RT, Skouteris D, Manolopoulos DE, Lee SH, Dong F, Liu K. 2000. Observation of a transition state resonance in the integral cross section of the F + HD reaction. *J. Chem. Phys.* 112:4536–52
9. Chao SD, Harich SA, Dai DX, Wang CC, Yang X, Skodje RT. 2002. A fully state- and angle-resolved study of the H + HD → D + H_2 reaction: comparison of a molecular beam experiment to ab initio quantum reaction dynamics. *J. Chem. Phys.* 117:8341–61
10. Skodje RT, Yang X. 2004. The

observation of quantum bottleneck states. *Int. Rev. Phys. Chem.* 23:253–87

11. Zewail AH. 2000. Femtochemistry: atomic-scale dynamics of the chemical bond. *J. Phys. Chem. A* 104:5660–94
12. Samson JAR, Gardner JL. 1973. Resonances in angular-distribution of Xenon photoelectrons. *Phys. Rev. Lett.* 31:1327–30
13. Dehmer JL, Dill D. 1976. Molecular effects on inner-shell photo absorption k-shell spectrum of N_2. *J. Chem. Phys.* 65:5327–34
14. Cooper JW. 1962. Photoionization from outer atomic subshells: a model study. *Phys. Rev.* 128:681–93
15. Fano U, Cooper JW. 1968. Spectral distribution of atomic oscillator strengths. *Rev. Mod. Phys.* 40:441–507
16. Suzuki T, Wang L, Kohguchi H. 1999. Femtosecond time-resolved photoelectron imaging on ultrafast electronic dephasing in an isolated molecule. *J. Chem. Phys.* 111:4859–61
17. Wang L, Kohguchi H, Suzuki T. 1999. Femtosecond time-resolved photoelectron imaging. *Faraday Discuss.* 113:37–46
18. Davies JA, LeClaire JE, Continetti RE, Hayden CC. 1999. Femtosecond time-resolved photoelectron-photoion coincidence imaging studies of dissociation dynamics. *J. Chem. Phys.* 111:1–4
19. Davies JA, Continetti RE, Chandler DW, Hayden CC. 2000. Femtosecond time-resolved photoelectron angular distributions probed during photodissociation of NO_2. *Phys. Rev. Lett.* 84:5983–86
20. Tsubouchi M, Whitaker BJ, Wang L, Kohguchi H, Suzuki T. 2001. Photoelectron imaging on time-dependent molecular alignment created by a femtosecond laser pulse. *Phys. Rev. Lett.* 86:4500–3
21. Bragg AE, Verlet JRR, Kammrath A, Cheshnovsky O, Neumark DM. 2004. Hydrated electron dynamics: from clusters to bulk. *Science* 306:669–71
22. Verlet JRR, Bragg AE, Kammrath A, Cheshnovsky O, Neumark DM. 2005. Observation of large water-cluster anions with surface-bound excess electrons. *Science* 307:93–96
23. Ramian G. *The World Wide Web Virtual Library: Free Electron Laser research and Applications*. http://sbfel3.ucsb.edu/www/vl_fel.html
24. Schotte F, Lim MH, Jackson TA, Smirnov AV, Soman J, et al. 2003. Watching a protein as it functions with 150-ps time-resolved X-ray crystallography. *Science* 300:1944–47
25. Plech A, Wulff M, Bratos S, Mirloup F, Vuilleumier R, et al. 2004. Visualizing chemical reactions in solution by picosecond X-ray diffraction. *Phys. Rev. Lett.* 92:125505
26. Neutze R, Huldt G, Hajdu J, van der Spoel D. 2004. Potential impact of an X-ray free electron laser on structural biology. *Radiat. Phys. Chem.* 71:905–16

26a. Zewail AH. 2006. 4D ultrafast electron diffraction, crystallography, and microscopy. *Annu. Rev. Phys. Chem.* 57:65–103

27. Amaldi U, Egidi A, Marconero R, Pizzella P. 1969. Use of a two channeltron coincidence in a new line of research in atomic physics. *Rev. Sci. Instrum.* 40:1001–4
28. Weigold E, Hood ST, Teubner PJO. 1973. Energy and angular correlations of the scattered and ejected electrons in the electron-impact ionization of Argon. *Phys. Rev. Lett.* 30:475–78
29. Takahashi M, Watanabe N, Khajuria Y, Udagawa Y, Eland JHD. 2005. Observation of a molecular frame (e, 2e) cross section: an (e, 2e + m) triple coincidence study on H_2. *Phys. Rev. Lett.* 94:213202
30. Itatani J, Levesque J, Zeidler D, Niikura H, Pepin H, et al. 2004. Tomographic imaging of molecular orbitals. *Nature* 432:867–71
31. Corkum PB. 1993. Plasma perspective on strong-field multiphoton ionization. *Phys. Rev. Lett.* 71:1994–97

32. Corkum PB, Ivanov MY, Wright JS. 1997. Subfemtosecond processes in strong laser fields. *Annu. Rev. Phys. Chem.* 48:387–406
33. Hentschel M, Kienberger R, Spielmann C, Reider GA, Milosevic N, et al. 2001. Attosecond metrology. *Nature* 414:509–13
34. Neumark DM. 2001. Time-resolved photoelectron spectroscopy of molecules and clusters. *Annu. Rev. Phys. Chem.* 52:255–77
35. Seideman T. 2002. Time-resolved photoelectron angular distributions: concepts, applications, and directions. *Annu. Rev. Phys. Chem.* 53:41–65
36. Reid KL. 2003. Photoelectron angular distributions. *Annu. Rev. Phys. Chem.* 54:397–424
37. Stolow A. 2003. Femtosecond time-resolved photoelectron spectroscopy of polyatomic molecules. *Annu. Rev. Phys. Chem.* 54:89–119
38. Wollenhaupt M, Engel V, Baumert T. 2005. Femtosecond laser photoelectron spectroscopy on atoms and small molecules: prototype studies in quantum control. *Annu. Rev. Phys. Chem.* 56:25–56
39. Hayden CC, Stolow A. 1999. Non-adiabatic dynamics studied by femtosecond time-resolved photoelectron spectroscopy. In *Photoionization and Photodetachment*, ed. C-Y Ng, pp. 91–126. Singapore: World Scientific
40. Radloff W. 1999. Femtosecond time-resolved photoelectron spectroscopy of molecules and clusters by photoion-photoelectron coincidence detection. In *Photoionization and Photodetachment*, ed. C-Y Ng, pp. 127–81. Singapore: World Scientific
41. Suzuki T, Whitaker BJ. 2001. Non-adiabatic effects in chemistry revealed by time-resolved charged-particle imaging. *Int. Rev. Phys. Chem.* 20:313–56
42. Suzuki T. 2004. Time-resolved photoelectron spectroscopy and imaging. In *Modern Trends in Chemical Reaction Dynamics: Experiment and Theory (Part I)*, ed. X Yang, K Liu, pp. 529–78. Singapore: World Scientific
43. Stolow A, Bragg AE, Neumark DM. 2004. Femtosecond time-resolved photoelectron spectroscopy. *Chem. Rev.* 104:1719–57
44. Dorner R, Mergel V, Jagutzki O, Spielberger L, Ullrich J, et al. 2000. Cold target recoil ion momentum spectroscopy: a “momentum microscope” to view atomic collision dynamics. *Phys. Rep.* 330:95–192
45. Ullrich J, Moshammer R, Dorn A, Dorner R, Schmidt LPH, Schmidt-Bocking H. 2003. Recoil-ion and electron momentum spectroscopy: reaction-microscope. *Rep. Prog. Phys.* 66:1463–545
46. Chandler DW, Houston PL. 1987. Two-dimensional imaging of state-selected photodissociation products detected by multiphoton ionization. *J. Chem. Phys.* 87:1445–47
47. Whitaker BJ, ed. 2003. *Imaging in Molecular Dynamics: Technology and Applications*. Cambridge: Cambridge Univ. Press
48. Wiley WC, McLaren IH. 1955. Time-of-flight mass spectrometer with improved resolution. *Rev. Sci. Instrum.* 26:1150–57
49. Helm H, Bjerre N, Dyer MJ, Huestis DL, Saeed M. 1993. Images of photoelectrons formed in intense laser fields. *Phys. Rev. Lett.* 70:3221–24
50. Kang WK, Kim YS, Jung KH. 1995. 2-dimensional photoelectron imaging of state-selected iodine atom by (2 + 1) resonance-enhanced multiphoton ionization. *Chem. Phys. Lett.* 244:183–87
51. Bordas C, Paulig F, Helm H, Huestis DL. 1996. Photoelectron imaging spectrometry: principle and inversion method *Rev. Sci. Instrum.* 67:2257–68
52. Eppink A, Parker DH. 1997. Velocity map imaging of ions and electrons using electrostatic lens: application in photoelectron and photofragment ion imaging of molecular oxygen. *Rev. Sci. Intrum.* 68:3477–84
53. Wrede E, Laubach S, Shultenburg S, Brown A, Wouters ER, et al. 2001.

Continuum state spectroscopy: a high resolution ion imaging study of IBr photolysis in the wavelength range 440–685 nm. *J. Chem. Phys.* 114:2629–46

54. Offerhaus HL, Nicole C, Lepine F, Bordas C, Rosca-Pruna F, Vrakking MJJ. 2001. A magnifying lens for velocity map imaging of electrons and ions. *Rev. Sci. Instrum.* 72:3245–48
55. Lebech M, Houver JC, Dowek D. 2002. Ion-electron velocity vector correlations in dissociative photoionization of simple molecules using electrostatic lenses. *Rev. Sci. Instrum.* 73:1866–74
56. Garcia GA, Nahon L, Harding CJ, Mikajlo EA, Powis I. 2005. A refocusing modified velocity map imaging electron/ion spectrometer adapted to synchrotron radiation studies. *Rev. Sci. Instrum.* 76:053302
57. Weber T, Weckenbrock M, Balser M, Schmidt L, Jagutzki O, et al. 2003. Auger electron emission from fixed-in-space CO. *Phys. Rev. Lett.* 90:153003
58. Sobottka SE, Williams MB. 1988. Delay line readout of microchannel plates. *IEEE Trans. Nucl. Sci.* 35:348–51
59. Li W, Chambreau SD, Lahankar SA, Suits AG. 2005. Megapixel ion imaging with standard video. *Rev. Sci. Instrum.* 76:063106
60. Chang BY, Hoetzlein RC, Mueller JA, Geiser JD, Houston PL. 1998. Improved two-dimensional product imaging: the real-time ion counting method. *Rev. Sci. Intrum.* 69:1665–70
61. Yonekura N, Gebauer C, Kohguchi H, Suzuki T. 1999. A crossed molecular beam apparatus using high-resolution ion imaging *Rev. Sci. Instrum.* 70:3265–70
62. Dribinski V, Ossadtchi A, Mandelshtam VA, Reisler H. 2002. Reconstruction of Abel-transformable images: the Gaussian basis-set expansion Abel transform method. *Rev. Sci. Instrum.* 73:2634–42
63. Garcia GA, Nahon L, Powis I. 2004. Two-dimensional charged particle image inversion using a polar basis function expansion. *Rev. Sci. Instrum.* 75:4989–96
64. Manzhos S, Loock HP. 2003. Photofragment image analysis using the onion-peeling algorithm. *Comput. Phys. Commun.* 154:76–87
65. Manzhos S, Loock HP. 2004. Photofragment image analysis via pattern recognition. *Rev. Sci. Instrum.* 75:2435–45
66. Arasaki Y, Takatsuka K, Wang K, McKoy V. 2000. Femtosecond energy- and angle-resolved photoelectron spectroscopy *J. Chem. Phys.* 112:8871–84
67. Arasaki Y, Takatsuka K, Wang K, McKoy V. 2003. Studies of electron transfer in NaI with pump-probe femtosecond photoelectron spectroscopy *J. Chem. Phys.* 119:7913–23
68. Felker PM, Zewail AH. 1987. Purely rotational coherence effect and time-resolved sub-Doppler spectroscopy of large molecules. I. Theoretical. *J. Chem. Phys.* 86:2460–82
69. Baskin JS, Felker PM, Zewail AH. 1987. Purely rotational coherence effect and time-resolved sub-Doppler spectroscopy of large molecules. II. Experimental. *J. Chem. Phys.* 86:2483–99
70. Yang CN. 1948. On the angular distribution in nuclear reactions and coincidence measurements. *Phys. Rev.* 74:764–72
71. Underwood JG, Reid KL. 2000. Time-resolved photoelectron angular distributions as a probe of intramolecular dynamics: connecting the molecular frame and the laboratory frame. *J. Chem. Phys.* 113:1067–74
72. Suzuki Y, Seideman T. 2005. Mapping rotational coherences onto time-resolved photoelectron imaging observables. *J. Chem. Phys.* 122:234302
73. Felker PM, Zewail AH. 1994. Molecular structure from ultrafast coherence spectroscopy. In *Femtosecond Chemistry*, ed. J Manz, L Wöste, pp. 193–260. New York: VCH Publishing
74. Bragg AE, Wester R, Davis AV, Kammrath A, Neumark DM. 2003. Excited-state detachment dynamics and rotational coherences of C_2^- via time-resolved

photoelectron imaging. *Chem. Phys. Lett.* 376:767–75

75. Bixon M, Jortner J. 1968. Intramolecular radiationless transitions. *J. Chem. Phys.* 48:715–26
76. Frad A, Lahmani F, Tramer A, Tric C. 1974. Luminescence and radiationless transitions from single vibronic level of the isolated pyrazine molecule in the S_1 (n, π^*) state. *J. Chem. Phys.* 60:4419–30
77. Lahmani F, Tramer A, Tric C. 1974. Nonexponential decays in single vibronic level fluorescence: a comparison between kinetics and quantum mechanical treatment. *J. Chem. Phys.* 60:4431–47
78. Kommandeur J, Majewski WA, Meerts WL, Pratt DW. 1987. Pyrazine: an "exact" solution to the problem of radiationless transitions. *Annu. Rev. Phys. Chem.* 38:433–62
79. McDonald DB, Fleming GR, Rice SA. 1981. Intermediate case radiationless decay: the excited state dynamics of pyrazine. *Chem. Phys.* 60:335–45
80. Yamazaki I, Murao T, Yamanaka T, Yoshihara K. 1983. Intramolecular electronic relaxation and photoisomerization processes in the isolated azabenzene molecules pyridine, pyrazine and pyrimidine. *Faraday Discuss.* 75:395–405
81. Knee JL, Doany FE, Zewail AH. 1985. Intramolecular dephasing in pyrazine: direct picosecond time resolution. *J. Chem. Phys.* 82:1042–43
82. Lorincz A, Smith DD, Novak F, Kosloff R, Tannor DJ, Rice SA. 1985. Rotational state dependence of pyrazine fluorescence: initial decays for the vibrationless $^1B_{3u}$ state. *J. Chem. Phys.* 82:1067–72
83. Felker PM, Zewail AH. 1986. Intramolecular dephasing in pyrazine: deuterium isotope effect and further tests of theory. *Chem. Phys. Lett.* 128:221–30
84. Suzuki T, Wang L, Tsubouchi M. 2004. Femtosecond photoelectron imaging on pyrazine: $(1 + 2')$ REMPI of deuterated pyrazine. *J. Phys. Chem. A* 108:5764–69
85. Song JK, Tsubouchi M, Suzuki T. 2001. Femtosecond photoelectron imaging on pyrazine: spectroscopy of 3s and 3p Rydberg states. *J. Chem. Phys.* 115:8810–18
86. Tsubouchi M, Whitaker BJ, Suzuki T. 2004. Femtosecond photoelectron imaging on pyrazine: $S_1 \rightarrow T_1$ intersystem crossing and rotational coherence transfer. *J. Phys. Chem. A* 108:6823–35
87. Innes K, Ross I, Moomaw W. 1988. Electronic states of azabenzenes and azanaphthalenes: a revised and extended critical review. *J. Mol. Spectrosc.* 132:492–544
88. Hougen JT. 1964. Rotational structure of singlet-triplet transition in near symmetric tops. *Can. J. Phys.* 42:433–51
89. Dill D. 1976. Fixed-molecule photoelectron angular distributions. *J. Chem. Phys.* 65:1130–33
90. Chandra N. 1987. Photoelectron spectroscopic studies. *J. Phys. B* 20:3405–15
91. Golovin AV. 1991. New method for measuring the angular distribution of electrons during dissociative photoionization of free oriented molecules: $O_2\,(X\,^3\Sigma_g^-) \rightarrow O_2^+\,(B\,^2\Sigma_g^-, v = 0\text{–}3) + e$. *Opt. Spektrosk.* 71:933–40
92. Shigemasa E, Adachi J, Oura M, Yagishita A. 1995. Angular distributions of $1s\sigma$ photoelectrons from fixed-in-space N_2 molecules *Phys. Rev. Lett.* 74:359–62
93. Hanold KA, Garner MC, Continetti RE. 1996. Photoelectron-photofragment angular correlation and energy partitioning in dissociative photodetachment. *Phys. Rev. Lett.* 77:3335–38
94. Downie P, Powis I. 1999. Molecule-frame photoelectron angular distributions from oriented CF_3I molecules. *Phys. Rev. Lett.* 82:2864–67
95. Hikosaka Y, Eland JHD, Watson TM, Powis I. 2001. Molecule frame photoelectron angular distributions from oriented methyl chloride and methyl fluoride molecules. *J. Chem. Phys.* 115:4593–603
96. Gessner O, Hikosaka Y, Zimmermann B, Hempelmann A, Lucchese RR, et al. 2002. 4 σ^{-1} inner valence photoionization dynamics of NO derived from

photoelectron-photoion angular correlations. *Phys. Rev. Lett.* 88:193002

97. Lebech M, Houver JC, Lafosse A, Dowek D, Alcaraz C, et al. 2003. Complete description of linear molecule photoionization achieved by vector correlations using the light of a single circular polarization. *J. Chem. Phys.* 118:9653–63
98. Dowek D, Lebech M, Houver JC, Lucchese RR. 2004. Photoemission in the molecular frame using the vector correlation approach: from valence to inner-valence shell ionization. *J. Electron Spectrosc. Relat. Phenom.* 141:211–27
99. Lucchese RR. 2004. A simple model for molecular frame photoelectron angular distributions. *J. Electron Spectrosc. Relat. Phenom.* 141:201–10
100. Rijs AM, Janssen MHM, Chrysostom ETH, Hayden CC. 2004. Femtosecond coincidence imaging of multichannel multiphoton dynamics. *Phys. Rev. Lett.* 92:123002
101. Ueda K, ed. 2004. *J. Electron Spectrosc. Relat. Phenom.*141:73–243
102. Allendorf SW, Leahy DJ, Jacobs DC, Zare RN. 1989. High-resolution angle-resolved and energy-resolved photoelectron-spectroscopy of NO: partial-wave decomposition of the ionization continuum. *J. Chem. Phys.* 91:2216–34
103. Reid KL, Leahy DJ, Zare RN. 1991. Effect of breaking cylindrical symmetry on photoelectron angular-distributions resulting from resonance-enhanced 2-photon ionization. *J. Chem. Phys.* 95:1746–56
104. Leahy DJ, Reid KL, Zare RN. 1991. Complete description of 2-photon $(1 + 1')$ ionization of NO deduced from rotationally resolved photoelectron angular distributions. *J. Chem. Phys.* 95:1757–67
105. Reid KL, Leahy DJ, Zare RN. 1992. Complete description of molecular photoionization from circular-dichroism of rotationally resolved photoelectron angular-distributions. *Phys. Rev. Lett.* 68:3527–30
106. Leahy DJ, Reid KL, Park HK, Zare RN. 1992. Measurement of circular-dichroism in rotationally resolved photoelectron angular-distributions following the photoionization of NO A $^2\Sigma^+$. *J. Chem. Phys.* 97:4948–57
107. Park H, Zare RN. 1993. Photoionization dynamics of the NO A $^2\Sigma^+$ state deduced from energy-resolved and angle-resolved photoelectron spectroscopy. *J. Chem. Phys.* 99:6537–44
108. Park H, Zare RN. 1996. Molecular-orbital decomposition of the ionization continuum for a diatomic molecule by angle- and energy-resolved photoelectron spectroscopy. I. Formalism. *J. Chem. Phys.* 104:4554–67
109. Park H, Zare RN. 1996. Molecular-orbital decomposition of the ionization continuum for a diatomic molecule by angle- and energy-resolved photoelectron spectroscopy. II. Ionization continuum of NO. *J. Chem. Phys.* 104:4568–80
110. Tsubouchi M, Suzuki T. 2004. Photoelectron kinetic energy dependence in near threshold ionization of NO from A state studied by time-resolved photoelectron imaging. *J. Chem. Phys.* 121:8846–53
111. Rudolph H, Dixit SN, McKoy V, Huo WH. 1988. Ionic rotational branching ratios in resonant enhanced multiphoton ionization of NO via the A $^2\Sigma^+$ (3sσ) and D $^2\Sigma^+$(3pσ) states *J. Chem. Phys.* 88:637–41
112. Wang K, Stephens JA, McKoy V. 1991. Effects of Cooper minima in resonance enhanced multiphoton ionization-photoelectron spectroscopy of NO via the D $^2\Sigma^+$ and C $^2\Pi$ Rydberg states *J. Chem. Phys.* 95:6456–62
113. Jungen C. 1970. Rydberg series in the NO spectrum: an interpretation of quantum defects and intensities in the s and d series. *J. Chem. Phys.* 53:4168–82
114. Fredin S, Gauyacq D, Horani M, Jungen C, Lefevre G, Masnouseeuws F. 1987. s and d Rydberg series of NO probed by double-resonance multiphoton

ionization: multichannel quantum defect analysis. *Mol. Phys.* 60:825–66

115. Hiyama M, Child MS. 2002. Ab initio R-matrix/multichannel quantum defect theory study of nitric oxide. *J. Phys. B* 35:1337–51
116. Guerout R, Jungen M, Jungen C. 2004. Ab initio molecular quantum defect theory. II. Rydberg and continuum states of NO. *J. Phys. B* 37:3057–73
117. Guerout R, Jungen M, Jungen C. 2004. Ab initio molecular quantum defect theory. I. Method of artificial well potentials. *J. Phys. B* 37:3043–55
118. Newton RG. 1982. *Scattering Theory of Waves and Particles*. New York: Springer
119. Seaton MJ. 1966. Quantum defect theory. I. General formulation. *Proc. Phys. Soc.* 88:801–14
120. Seaton MJ. 1966. Quantum defect theory. II. Illustrative one-channel and two-channel problems. *Proc. Phys. Soc.* 88:815–32
121. Rosenberg L. 1995. Levinson-Seaton theorem for potentials with an attractive Coulomb tail. *Phys. Rev. A* 52:3824–26
122. Rosenberg L. 1996. Bound-state methods for low-energy electron-ion scattering. *Phys. Rev. A* 53:791–97
123. Motoki S, Adachi J, Ito K, Ishii K, Soejima K, et al. 2002. Complete photoionization experiment in the region of the 2 $\Delta_g \rightarrow \Delta_u$ shape resonance of the N_2 molecule. *J. Phys. B* 35:3801–19
124. Cherepkov NA, Raseev G, Adachi J, Hikosaka Y, Ito K, et al. 2000. K-shell photoionization of CO. II. Determination of dipole matrix elements and phase differences. *J. Phys. B* 33:4213–36
125. Loesh HJ, Remscheid A. 1990. Brute force in molecular reaction dynamics: a novel technique for measuring steric effects. *J. Chem. Phys.* 93:4779–90
126. Friedrich B, Hershbach DR. 1991. On the possibility of orienting rotationally cooled polar-molecules in an electric-field *Z. Phys. D At. Mol. Clusters* 18:153–61
127. Wu M, Bemish RJ, Miller RE. 1994. Photodissociation of molecules oriented by DC electric fields: determining photofragment angular distributions. *J. Chem. Phys.* 101:9447–56
128. Friedrich B, Hershbach DR. 1995. Alignment and trapping of molecules in intense laser fields *Phys. Rev. Lett.* 74:4623–26
129. Friedrich B, Hershbach DR. 1995. Polarization of molecules induced by intense nonresonant laser fields *J. Phys. Chem.* 99:15686–93
130. Seideman T. 1995. Rotational excitation and molecular alignment in intense laser fields. *J. Chem. Phys.* 103:7887–96
131. Kim W, Felker PM. 1996. Spectroscopy of pendular states in optical-field-aligned species. *J. Chem. Phys.* 104:1147–50
132. Seideman T. 1999. Revival structure of aligned rotational wave packets *Phys. Rev. Lett.* 83:4971–74
133. Rosca-Pruna F, Vrakking MJJ. 2001. Experimental observation of revival structures in picosecond laser-induced alignment of I_2. *Phys. Rev. Lett.* 87:153902
134. Ortigoso J, Rodríguez M, Gupta M, Friedrich B. 1999. Time evolution of pendular states created by the interaction of molecular polarizability with a pulsed nonresonant laser field. *J. Chem. Phys.* 110:3870–75
135. Tsubouchi M, Suzuki T. 2005. Photoionization of homonuclear diatomic molecules aligned by an intense femtosecond laser pulse. *Phys. Rev. A* 72:022512
136. Dooley PW, Litvinyuk IV, Lee KF, Rayner DM, Spanner M, et al. 2003. Direct imaging of rotational wave-packet dynamics of diatomic molecules. *Phys. Rev. A* 68:023406
137. Averbukh IS, Arvieu R. 2001. Angular focusing, squeezing, and rainbow formation in a strongly driven quantum rotor. *Phys. Rev. Lett.* 87:163601
138. Leibscher M, Averbukh IS, Rabitz H. 2003. Molecular alignment by trains of short laser pulses. *Phys. Rev. Lett.* 90:213001
139. Leibscher M, Averbukh IS, Rabitz H.

2004. Enhanced molecular alignment by short laser pulses. *Phys. Rev. A* 69:013402

140. Bisgaard CZ, Poulson MD, Péronne E, Viftrup SS, Stapelfeldt H. 2004. Observation of enhanced field-free molecular alignment by two laser pulses. *Phys. Rev. Lett.* 92:173004
141. Lee KF, Litvinyuk IV, Dooley PW, Spanner M, Villeneuve DM, Corkum PB. 2004. Two-pulse alignment of molecules. *J. Phys. B* 37:L43–48
142. Péronne E, Poulson MD, Stapelfeldt H, Bisgaard CZ, Hamilton E, Seideman T. 2004. Nonadiabatic laser-induced alignment of iodobenzene molecules *Phys. Rev. A* 70:063410
143. Péronne E, Poulsen MD, Bisgaard CZ, Stapelfeldt H, Seideman T. 2003. Nonadiabatic alignment of asymmetric top molecules: field-free alignment of iodobenzene. *Phys. Rev. Lett.* 91:043003
144. Underwood JG, Spanner M, Ivanov MY, Mottershead J, Sussman BJ, Stolow A. 2003. Switched wave packets: a route to nonperturbative quantum control. *Phys. Rev. Lett.* 90:223001
145. Underwood JG, Sussman BJ, Stolow A. 2005. Field-free three dimensional molecular axis alignment. *Phys. Rev. Lett.* 94:143002
146. Itatani J, Zeidler D, Levesque J, Spanner M, Villeneuve DM, Corkum PB. 2005. Controlling high harmonic generation with molecular wave packets. *Phys. Rev. Lett.* 94:123902
147. Kennedy DJ, Manson ST. 1972. Photoionization of the noble-gases: cross sections and angular distributions. *Phys. Rev. A* 5:227–47
148. Dehmer JL, Dill D. 1975. Shape resonances in K-shell photoionization of diatomic molecules. *Phys. Rev. Lett.* 35:213–15
149. Piancastelli MN, Keller PR, Taylor JW, Grimm FA, Carlson TA. 1983. Angular distribution parameter as a function of photon energy for some mono- and diazabenzenes and its use for orbital assignment. *J. Am. Chem. Soc.* 105:4235–39
150. Dill D, Dehmer JL. 1974. Electron-molecule scattering and molecular photoionization using the multiple-scattering method. *J. Chem. Phys.* 61:692–99
151. Suzuki Y, Suzuki T. 2006. Photoelectron angular distribution of heteroaromatic molecules studied by a continuum multiple scattering Xα method. Submitted.
152. Baltzer P, Karlsson L, Wannberg, Öhrwall G, Holland DMP, et al. 1997. An experimental and theoretical study of the valence shell photoelectron spectrum of the benzene molecule *Chem. Phys.* 224:95–119
153. Carlson TA, Gerard P, Krause MO, Grimm FA, Pullen BP. 1987. Photoelectron dynamics of the valence shells of benzene as a function of photon energy. *J. Chem. Phys.* 86:6918–26
154. Bellm SM, Reid KL. 2003. Reevaluation of the use of photoelectron angular distributions as a probe of dynamical processes: strong dependence of such distributions from S_1 paradifluorobenzene on photoelectron kinetic energy. *Phys. Rev. Lett.* 91:263002
155. Bellm SM, Davies JA, Whiteside PT, Guo J, Powis I, Reid KL. 2005. An unusual π^* shape resonance in the near-threshold photoionization of S_1 para-difluorobenzene. *J. Chem. Phys.* 122:224306
156. Cacelli I, Carravetta V, Rizzo A, Moccia R. 1991. The calculation of photoionization cross-sections of simple polyatomic-molecules by L^2 methods *Phys. Rep.* 205:283–351
157. Lucchese RR, Takatsuka K, McKoy V. 1985. Applications of the Schwinger variational principle to electron molecule collisions and molecular photoionization *Phys. Rep.* 131:147–221
158. Burke PG, Berrington KA, eds. 1993. *Atomic and Molecular Processes: An R-Matrix Approach.* Bristol: Institute of Physics

159. Gianturco FA, Lucchese RR. 2001. Cross sections and asymmetry parameters in gas-phase photoionization of C_{60}. *Phys. Rev. A* 64:032706
160. Stener M, Furlan S, Decleva P. 2001. Density functional calculations of valence and core photoionization of C_6H_6 with an exchange-correlation potential with the correct asymptotic behavior. *Phys. Chem. Chem. Phys.* 3:19–28
161. Stener M, Fronzoni G, Decleva P. 2005. Time-dependent density-functional theory for molecular photoionization with noniterative algorithm and multicenter B-spline basis set: CS_2 and C_6H_6 case studies. *J. Chem. Phys.* 122:234301
162. Surber E, Mabbs R, Sanov A. 2003. Probing the electronic structure of small molecular anions by photoelectron imaging. *J. Phys. Chem. A* 107:8215–24
163. Mabbs R, Surber E, Sanov A. 2005. Photoelectron anisotropy and channel branching ratios in the detachment of solvated iodide cluster anions. *J. Chem. Phys* 122:054308
164. Cooper J, Zare RN. 1968. Angular distribution of photoelectrons. *J. Chem. Phys.* 48:942–43
165. Cooper J, Zare RN. 1968. Erratum: angular distribution of photoelectrons. *J. Chem. Phys.* 49:4252
166. Radojevic V, Kelly HP, Johnson WR. 1987. Photodetachment of negative halogen ions. *Phys. Rev. A* 35:2117–21
167. Hanstrop D, Bengtsson C, Larson DJ. 1989. Angular distributions in photodetachment from O^-. *Phys. Rev. A* 40:670–75
168. Wigner EP. 1948. On the behavior of cross sections near thresholds. *Phys. Rev.* 73:1002–9
169. Zanni MT, Batista VS, Greenblatt BJ, Miller WH, Neumark DM. 1999. Femtosecond photoelectron spectroscopy of the I_2^- anion: characterization of the $\tilde{A}'\ {}^2\Pi_{g,1/2}$ excited state. *J. Chem. Phys.* 110:3748–55
170. Batista VS, Zanni MT, Greenblatt BJ, Neumark DM, Miller WH. 1999. Femtosecond photoelectron spectroscopy of I_2^- anion: a semiclassical molecular dynamics simulation method. *J. Chem. Phys.* 110:3736–47
171. Davis AV, Wester R, Bragg AE, Neumark DM. 2003. Time-resolved photoelectron imaging of the photodissociation of I_2^-. *J. Chem. Phys.* 118:999–1002
172. Mabbs R, Pichugin K, Sanov A. 2005. Dynamic molecular interferometer: probe of inversion symmetry in I_2^- photodissociation. *J. Chem. Phys.* 123:054329
173. Siegbahn H, Siegbahn K. 1973. ESCA applied to liquids. *J. Electron Spectrosc. Rel. Phenom.* 2:319–25
174. Siegbahn H. 1985. Electron-spectroscopy for chemical-analysis of liquids and solutions *J. Phys. Chem.* 89:897–909
175. Faubel M, Steiner B, Toennies JP. 1997. Photoelectron spectroscopy of liquid water, some alcohols, and pure nonane in free micro jets. *J. Chem. Phys.* 106:9013–31
176. Faubel M, Steiner B, Toennies JP. 1998. Measurement of He I photoelectron spectra of liquid water, formamide and ethylene glycol in fast-flowing microjets. *J. Electron Spectrosc. Rel. Phenom.* 95:159–69
177. Faubel M. 1999. Photoelectron spectroscopy at liquid surfaces. In *Photoionization and Photodetachment*, ed. C-Y Ng, pp. 634–90. Singapore: World Scientific
178. Weber R, Winter B, Schmidt PM, Widdra W, Hertel IV, et al. 2004. Photoemission from aqueous alkali-metal-iodide salt solutions using EUV synchrotron radiation. *J. Phys. Chem. B* 108:4729–36
179. Winter B, Weber R, Schmidt PM, Hertel IV, Faubel M, et al. 2004. Molecular structure of surface-active salt solutions: photoelectron spectroscopy and molecular dynamics simulations of aqueous tetrabutylammonium iodide. *J. Phys. Chem. B* 108:14558–64
180. Winter B, Weber R, Widdra W, Dittmar

M, Faubel M, Hertel IV. 2004. Full valence band photoemission from liquid water using EUV synchrotron radiation. *J. Phys. Chem. A* 108:2625–32

181. Winter B, Weber R, Hertel IV, Faubel M, Jungwirth P, et al. 2005. Electron binding energies of aqueous alkali and halide ions: EUV photoelectron spectroscopy of liquid solutions and combined ab initio and molecular dynamics calculations. *J. Am. Chem. Soc.* 127:7203–14
182. Yokoyama K, Silva C, Son DH, Walhout PK, Barbara PF. 1998. Detailed investigation of the femtosecond pump-probe spectroscopy of the hydrated electron. *J. Phys. Chem. A* 102:6957–66
183. Silva C, Walhout PK, Yokoyama K, Barbara PF. 1998. Femtosecond solvation dynamics of the hydrated electron. *Phys. Rev. Lett.* 80:1086–89
184. Baltuska A, Emde MF, Pshenichnikov MS, Wiersma DA. 1999. Early-time dynamics of the photoexcited hydrated electron. *J. Phys. Chem. A* 103:10065–82
185. Tauber MJ, Mathies RA. 2003. Structure of the aqueous solvated electron from resonance Raman spectroscopy: lessons from isotopic mixtures. *J. Am. Chem. Soc.* 125:1394–402
186. Pshenichnikov MS, Baltuska A, Wiersma DA. 2004. Hydrated-electron population dynamics. *Chem. Phys. Lett.* 389:171–75
187. Thaller A, Laenen R, Laubereau A. 2004. Femtosecond spectroscopy of the hydrated electron: novel features in the infrared. *Chem. Phys. Lett.* 398:459–65
188. Mizuno M, Yamaguchi S, Tahara T. 2005. Relaxation dynamics of the hydrated electron: femtosecond time-resolved resonance Raman and luminescence study. *J. Phys. Chem. A* 109:5257–65
189. Paik DH, Lee IR, Yang DS, Baskin JS, Zewail AH. 2004. Electrons in finite-sized water cavities: hydration dynamics observed in real time. *Science* 306:672–75

Annual Review of Physical Chemistry
Volume 57, 2006

CONTENTS

INDEXES

ERRATA

An online log of corrections to *Annual Review of Physical Chemistry* chapters may be found at http://physchem.annualreviews.org/errata.shtml